International Journal of Nanomedicine

Dovepress
open access to scientific and medical research

Open Access Full Text Article

ORIGINAL RESEARCH

Engineering Ag-Decorated Graphene Oxide Nano-Photothermal Platforms with Enhanced Antibacterial Properties for Promoting Infectious Wound Healing

Zhiwei Sun[1,*], Xiangru Chen[1,*], Fang Miao[2,*], Na Meng[3], Keqiang Hu[1], Shaotang Xiong[4], Ximing Peng[1], Liya Ma[5], Chuchao Zhou[1], Yanqing Yang[1]

[1]Department of Plastic Surgery, Tongren Hospital of Wuhan University (Wuhan Third Hospital), Wuhan, 430060, People's Republic of China; [2]Department of Dermatology, Renmin Hospital of Wuhan University, Wuhan, 430060, People's Republic of China; [3]Department of Cardiovascular Medicine, Tongren Hospital of Wuhan University (Wuhan Third Hospital), Wuhan, 430060, People's Republic of China; [4]The Second People's Hospital of China Three Gorges University·the Second People's Hospital of Yichang, Hubei, People's Republic of China; [5]The Centre of Analysis and Measurement of Wuhan University, Wuhan University, Wuhan, 430072, People's Republic of China

*These authors contributed equally to this work

Correspondence: Yanqing Yang; Chuchao Zhou, Email yangyq0106@163.com; chuchaozhou@163.com

Introduction: Graphene oxide (GO) nanoparticles have emerged as a compelling photothermal agent (PHTA) in the realm of photothermal antibacterial therapy, owing to their cost-effectiveness, facile synthesis, and remarkable photostability. Nevertheless, the therapeutic efficacy of GO nanoparticles is commonly hindered by their inherent drawback of low photothermal conversion efficiency (PCE).

Methods: Herein, we engineer the Ag/GO-GelMA platform by growing the Ag on the surface of GO and encapsulating the Ag/GO nanoparticles into the GelMA hydrogels.

Results: The resulting Ag/GO-GelMA platform demonstrates a significantly enhanced PCE (47.6%), surpassing that of pure GO (11.8%) by more than fourfold. As expected, the Ag/GO-GelMA platform, which was designed to integrate the benefits of Ag/GO nanoparticles (high PCE) and hydrogel (slowly releasing Ag^+ to exert an inherent antibacterial effect), has been shown to exhibit exceptional antibacterial efficacy. Furthermore, transcriptome analyses demonstrated that the Ag/GO-GelMA platform could significantly down-regulate pathways linked to inflammation (the MAPK and PI3K-Akt pathways) and had the ability to promote cell migration.

Discussion: Taken together, this study presents the design of a potent photothermal antibacterial platform (Ag/GO-GelMA) aimed at enhancing the healing of infectious wounds. The platform utilizes a handy method to enhance the PCE of GO, thereby making notable progress in the utilization of GO nano-PHTAs.

Keywords: Ag/GO nanoparticles, photothermal therapy, photothermal conversion efficiency, hydrogel, infectious wound healing

Introduction

The skin tissue, being the largest and most exposed tissue in the human body, is also the most vulnerable. The repair process of damaged skin tissue is notably intricate.[1] Wound infection emerges as a fundamental factor that impedes and prolongs the healing process. In order to ensure the efficacy of antibiotics in combating and preventing wound infections, it is imperative to achieve a high concentration specifically at the site of the wound. This localized concentration should be prioritized over systemic administration, which can result in severe side effects due to elevated serum levels.[2] Simultaneously, the inappropriate utilization, particularly the excessive usage of antibiotics, has resulted in the emergence of numerous multidrug-resistant (MDR) bacteria.[3] Currently, numerous studies have focused on enhancing skin

Received: 19 June 2024
Accepted: 22 August 2024
Published: 30 August 2024

Graphical Abstract

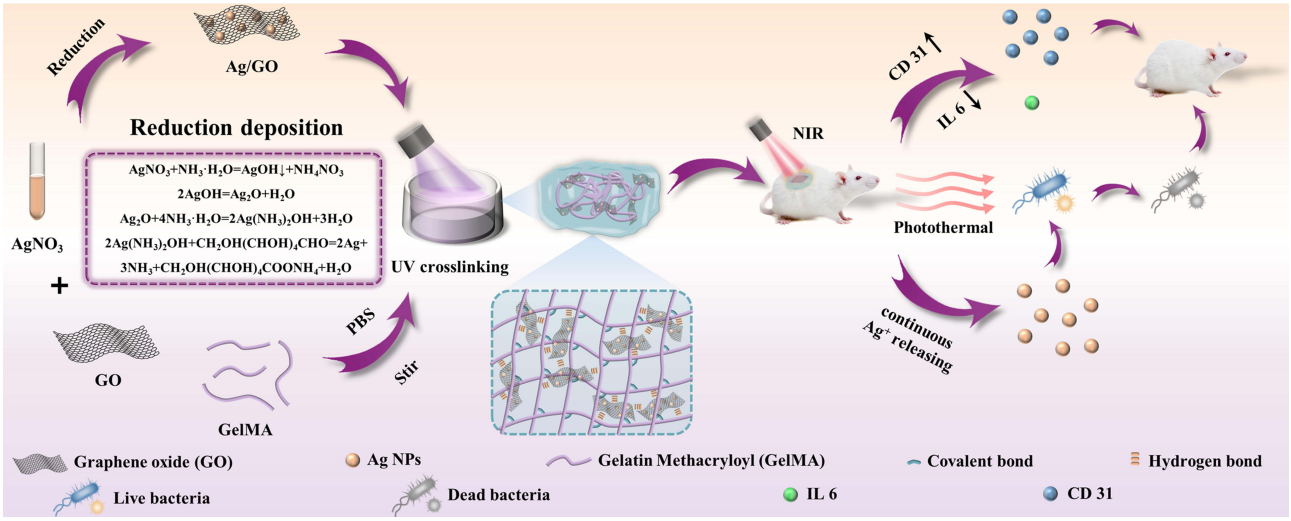

regeneration for the treatment of various refractory wounds. For instance, Shafiq et al developed a core/shell fiber incorporating bioactive peptides, which demonstrated a significant capacity to promote wound healing.[4] Similarly, Yuan et al engineered a multifunctional nanofiber dressing capable of inducing macrophage polarization and inhibiting inflammation by facilitating wound re-epithelialization and neovascularization, thereby promoting scar-free wound healing.[5] Nevertheless, additional therapeutic strategies are required to address the challenge of multi-resistant bacterial infections. Consequently, the pursuit of powerful alternative therapeutics to eliminate bacterial infections without provoking multidrug resistance has become a pressing objective.

Light is a highly advantageous instrument that has significantly influenced contemporary medicine.[6] encompassing drug administration, photothermal therapy (PTT), photodynamic therapy (PDT), and tissue engineering.[7] This can be attributed to its convenient application, noninvasive characteristics, and ability to be controlled in terms of space and time.[8] Numerous investigations have demonstrated that localized hyperthermia induced by photothermal agents (PHTAs) under the illumination of light at a specific wavelength can lead to the disruption of bacterial integrity, rendering it a widely employed approach in the management of wounds accompanied by bacterial infection.[9] Among the various therapeutic approaches, PTT involves artificially elevating tissue temperature through the utilization of PHTAs.[10] These agents possess the ability to absorb light and subsequently convert it into heat, thereby inducing protein denaturation, cell cavitation and rupture, bubble formation, and DNA fragmentation.[11] Consequently, this process facilitates the thermal ablation of undesirable cells at the intended location, ultimately yielding a favorable therapeutic outcome.[10,11] PTT, due to its high inherent specificity and low invasive burden, presents itself as a compelling and auspicious method for localized heating.[12] This technique effectively enhances blood circulation within the wound vicinity, concurrently promoting fibroblast proliferation and mitigating inflammation. Consequently, PTT expedites the overall wound-healing process.[13]

A range of inorganic materials, including gold nanoparticles, carbon nanomaterials, transitional metal dichalcogenide, and palladium nanosheets, along with organic nanoparticles such as polyaniline, porphyrins, polydopamine, cyanines, and polypyrrole, are currently under development as potential PHTAs for PTT.[14] Among these materials, graphene oxide (GO) has gained significant attention as a promising PHTAs in PTT, owing to its excellent photostability, low cost, and favorable compatibility.[15] In recent years, researchers have designed GO nanomaterials of different sizes (ranging from 20 to 500 nm) for PTT.[16] However, there are two main defects associated with the currently developed GO nano-PHTAs. To begin with, akin to numerous other inorganic nanomaterials, GO exhibits a relatively low photothermal conversion

efficiency (PCE) of approximately 15% upon exposure to 808 nm near-infrared (NIR) laser irradiation. Moreover, the PCE diminishes further at longer wavelengths, primarily attributed to incomplete nonradiative transitions, thereby resulting in feeble NIR absorbability, which results in the use of higher near-infrared laser power and longer laser irradiation time when PTT is performed with PHTAs. For instance, Chen et al utilized PTT to facilitate diabetic wound healing, but their required laser power and irradiation time were 1.5 W cm^{-2} and 5 minutes, respectively.[17] Yan et al utilized PTT to promote infectious wound healing, but the laser power and irradiation time they needed were also 2.0 W cm^{-2} and 5 minutes, respectively.[18] Another noteworthy aspect pertains to the propensity of GO nanomaterials to aggregate easily, owing to the presence of a substantial number of active moieties such as hydroxyl (–OH) and carboxyl (–COOH) groups on the surface of nano-GO.[19,20] The emergence and aggregation of GO nanomaterials have been found to have a detrimental effect on light absorbance efficiency, leading to a subsequent decrease in PCE. These two drawbacks significantly impede the practical utilization of GO-based nano-PHTAs in various applications.[21] The previous study of Tan et al prepared enhanced synergistic antibacterial RGO/Ag nanocomposites but failed to solve the problem of their easy aggregation.[15] Consequently, the simultaneous enhancement of light absorption efficiency and reduction of nanomaterial aggregation poses major challenges in the development of high-performance GO-based PHTAs for the treatment of bacterial infections.

Extensive endeavors have been undertaken to enhance the PCE of GO nanomaterials through two approaches: enhancing light absorption efficiency by minimizing nonradiative transitions in the NIR region and facilitating the nanomaterials' dispersion by introducing a suitable carrier. For example, Cheng et al demonstrated that in situ growth of metal nanoparticles on the surfaces of PHTAs enhanced the photothermal performance due to improved charge transfer efficiency, which then induced enhanced nonradiative transitions.[22] Shen et al have shown that Ag ions can improve the PCE of GO, but no further applications have been made.[23] Zeng et al found that loading PHTAs in a hydrogel matrix reduced aggregation, resulting in high PTT efficiency.[24] These findings serve as a reminder that the incorporation of metal nanoparticles onto GO, followed by its encapsulation within a hydrogel scaffold, has the potential to enhance the photothermal properties of GO.

In order to test the aforementioned hypothesis, we have developed a biocompatible hydrogel that contains Ag/GO nanoparticles for potential use in treating focal infections. Figure 1 illustrates the successful growth of Ag nanoparticles on the surface of GO nanoparticles using the reduction-deposition method. The addition of Ag resulted in a significant improvement in the photothermal conversion rate, increasing it from 11.8% (for GO) to 46.2% (for Ag/GO). Subsequently, the Ag/GO nanoparticles were incorporated into the Gelatin Methacryloyl (GelMA) hydrogel network using a simple one-pot blending technique combined with UV-crosslinking, resulting in the formation of the Ag/GO-GelMA hydrogel. The addition of a hydrogel carrier first achieved uniform dispersion of Ag/GO nanoparticles and effectively prevented agglomeration. Therefore, the combination of Ag/GO-GelMA systems can improve the PCE from 46.2% to 47.6%. Secondly, the GelMA hydrogel exhibits the ability to slowly release Ag^{+}, thereby mitigating their oxidation and extending their antibacterial efficacy. Consequently, the GelMA hydrogel offers an extra antibacterial effect. In vitro antibacterial tests have demonstrated that the Ag/GO-GelMA hydrogel possesses a broad-spectrum antibacterial property, effectively inhibiting the growth of Escherichia coli (*E. coli*) by 99.9% and Staphylococcus aureus (*S. aureus*) by 99.9%. Additional findings demonstrated that the Ag/GO-GelMA hydrogel exhibited remarkable bactericidal efficacy in an in vivo rat wound infection model, thereby facilitating the expedited healing process of infected wounds (with a wound healing rate of 94.34%±1.71% on day 12). Histological staining further revealed a reduction in IL-6 levels and an increase in CD31 levels. Subsequent sequencing and bioinformatics analysis revealed its regulatory role in the IL-17 signaling pathway and its activation of the MAPK pathway, thereby facilitating the healing process of infected wounds through the down-regulation of IL-6. This study presents novel insights into the development of a resilient GO-based photothermal system for antibacterial therapy and wound healing.

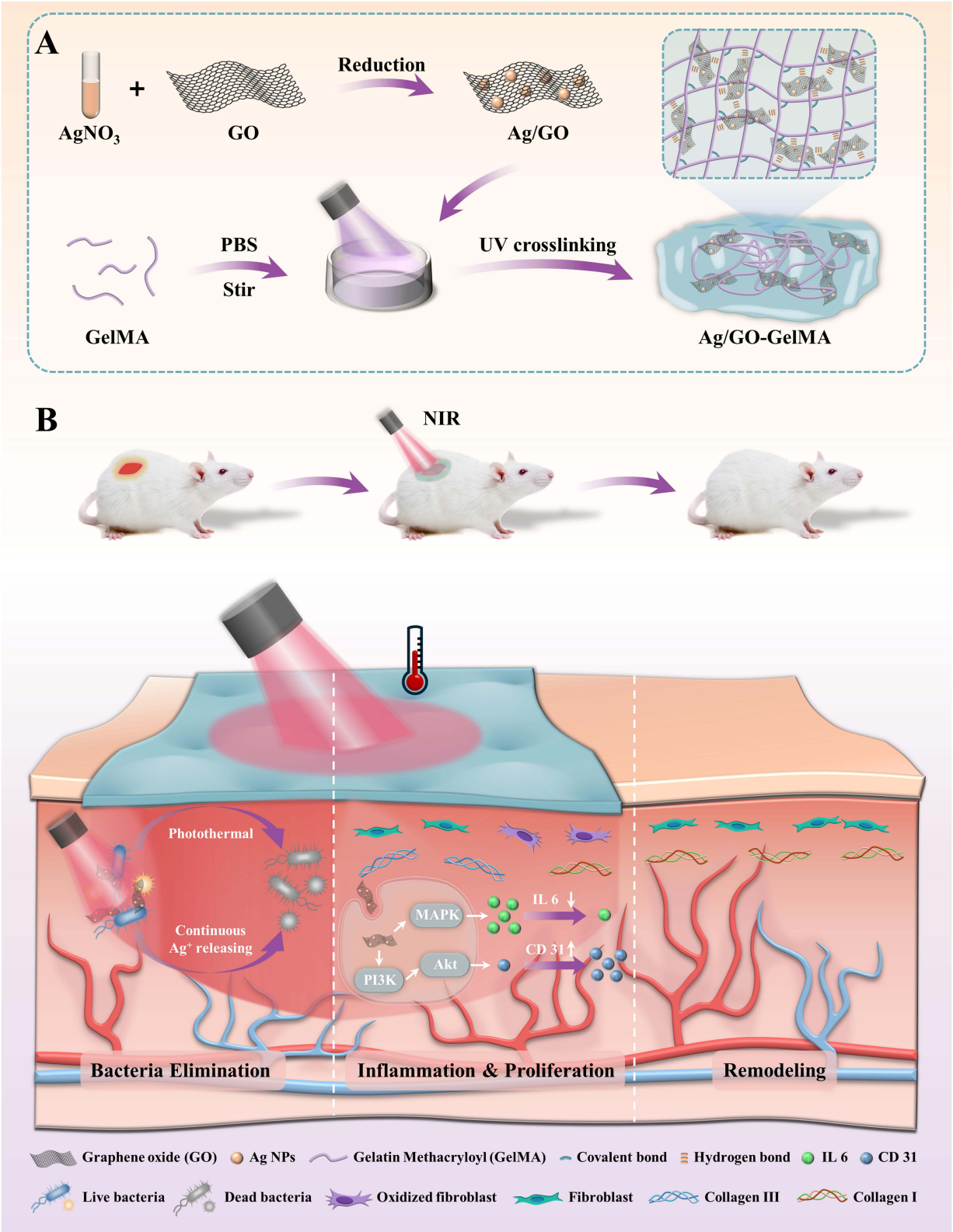

Figure 1 This schematic illustrates the fabrication of Ag/GO-GelMA hydrogel and its use as an antibacterial wound dressing using PTT. (**A**) Using reduction-deposition and UV-crosslinking approaches, (**B**) we easily constructed a potent hydrogel dressing that can attenuate wound infection through synergistic antibacterial therapies such as photothermal effect and continuous Ag^+ releasing, regulate inflammation and angiogenesis through MAPK signaling pathway and PI3K-AKT signaling pathway, and promote cell migration, thereby ultimately accelerating infectious wound healing.

Results and Discussion

Fabrication and Physicochemical Characterization of Ag/GO Nanoparticles

In this study, Ag/GO nanoparticles were prepared using a reduction-deposition method, as depicted in Figure 1. The selection of Ag nanoparticles for deposition was based on their favorable photoelectric properties, which have the potential to reduce the nonradiative transition through charge transfer and increase the near-infrared absorption,[25] thus enhancing the PCE of the designed nanoparticles (Figure 2A). During the fabrication process, the various functional groups present on the surface of GO, such as OH groups and COOH groups, actively engaged in the reduction-deposition of Ag ions, resulting in the formation of Ag and the establishment of coordination linkages with Ag NPs.[26]

The morphology of the designed Ag/GO nanoparticles was initially assessed using scanning electron microscopy (SEM) (Figure 2B) and transmission electron microscopy (TEM) (Figure 2C). The GO nanoparticles exhibited a relatively uniform distribution of Ag nanoparticles with an average diameter of 50 nm on their surface. Then, as shown in Figure 2D, the zeta potentials of the nanoparticles changed from −31.1 mV (GO) to −21.6 mV (Ag/GO) due to the reduction of Ag^+ into Ag NPs which resulted in the consumption of a certain quantity of negatively charged groups of GO. What's more, after Ag NPs were loaded on the surface of GO NPs, the zeta potentials of the nanoparticles changed from −1.1 mV (Ag) to −21.6 mV (Ag/GO), indicating that GO NPs increased the dispersion of Ag NPs and reduced its deposition.[21] Furthermore, a comparison was made between the X-ray diffraction (XRD) pattern of Ag/GO NPs and that of GO NPs. The XRD pattern of GO revealed a distinct peak at $2\theta = 9.8°$, indicating its characteristic properties, as depicted in Figure 2E. In the XRD of Ag/GO, the presence of metallic Ag was observed through the peaks of Ag (111) at 38.2°, Ag (200) at 44.4°, Ag (220) at 64.4°, and Ag (311) at 77.5°.[27] Additionally, SEM-assisted element mapping images were utilized to confirm the successful construction of Ag/GO NPs, revealing the homogeneous distribution of C, O, and Ag elements, as shown in Figure 2F. Afterward, the UV–vis–NIR absorption spectra of the as-prepared GO and Ag/GO NPs were examined. It is well-established that Ag NPs exhibit a surface plasmon resonance band at approximately 440 nm, which can be detected through UV –vis –NIR spectroscopy. Consistent with expectations, the Ag/GO NPs' absorption at 808 nm was significantly greater than that of GO, potentially attributed to the UV absorption contributed by Ag.[28] This observation implies that Ag/GO may be more suitable for photothermal therapy (PTT), as depicted in Figure 2G. Other researchers have also reported a comparable increase in spectral absorption due to the deposition of Ag nanoparticles.[29] It is worth noting that the photothermal conversion efficiency (η) of GO and Ag/GO at 808 nm was determined to be 11.8% and 46.2% (Figure 2H and I), using Equations (4)–(6). According to these results, the hybrid system's photothermal performance improved significantly after Ag deposition.[30]

$$\eta = \frac{hA(T_{max,sam} - T_{max,water})}{I\left(1 - 10^{-A_{808}}\right)} \tag{1}$$

$$t = \frac{\sum_i m_i C_{P,i}}{hA} ln\theta \tag{2}$$

$$\theta = \frac{T - T_{sur}}{T_{max} - T_{sur}} \tag{3}$$

where $T_{max,sam}$ denotes the maximum temperature generated by samples; $T_{max,water}$ denotes the maximum temperature generated by water; I denotes the laser power; A_{808} denotes the absorbance of the aqueous solution of samples at 808 nm; m_i denotes the weight of water; $C_{p,i}$ denotes the heat capacity of water; and θ denotes the system constant.[31]

Fabrication and Physicochemical Characterization of Ag/GO-GelMA Hydrogels

In order to enhance the biocompatibility and photothermal performance of Ag/GO nanoparticles, three Ag/GO-GelMA hydrogels (1AGG, 2AGG, and 5AGG) were synthesized using an environmentally approachable one-pot mixing and UV-crosslinking method. The GelMA solution was combined with Ag/GO nanoparticles, resulting in a rapid sol-gel transition facilitated by UV light-induced crosslinking (Figure S1). Simultaneously, the GelMA networks engage in numerous noncovalent interactions with anionic Ag/GO nanoparticles, encompassing hydrogen bonding, π–π stacking,

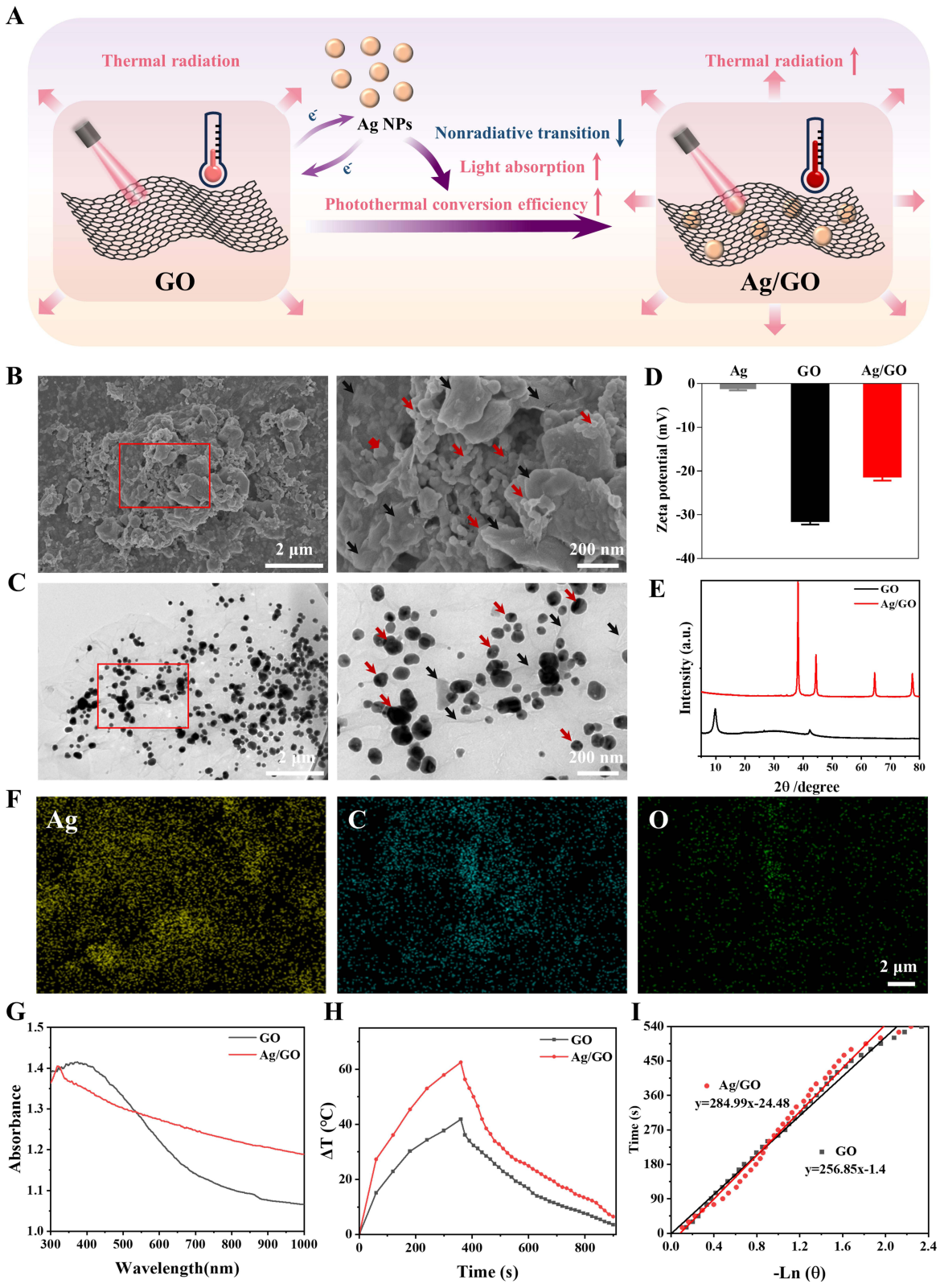

Figure 2 Characterization of Ag/GO nanoparticles. (**A**) Schematic illustration of the improved PCE of GO nanoparticles loaded with Ag NPs. (**B**) SEM images, (**C**) TEM images, and (**E**) XRD patterns of GO and Ag/GO NPs. (The red arrow refers to Ag/GO NPs and black arrow refers to GO NPs). (**D**) zeta potentials of Ag, GO, and Ag/GO NPs, (**F**) SEM elemental mapping images of Ag, C, and O of Ag/GO NPs. (**G**) UV–vis–NIR absorption spectra, (**H**) photothermal effects, and (**I**) the cooling time is plotted against the negative natural logarithm of the driving force temperature during the cooling of GO and Ag/GO nanoparticles.

and electrostatic forces. These reversible non-covalent bonds confer a specific self-healing capability upon the synthesized hydrogel, thereby enhancing the practicality of Ag/GO-GelMA hydrogels for photothermal applications. Furthermore, the incorporation of GO nanoparticles into the GelMA matrix resulted in a transition of the hydrogel's color from transparent to brown, as observed in Figure 3A and Figure S2A. Similarly, the introduction of Ag/GO nanoparticles caused the hydrogel to exhibit a black coloration.

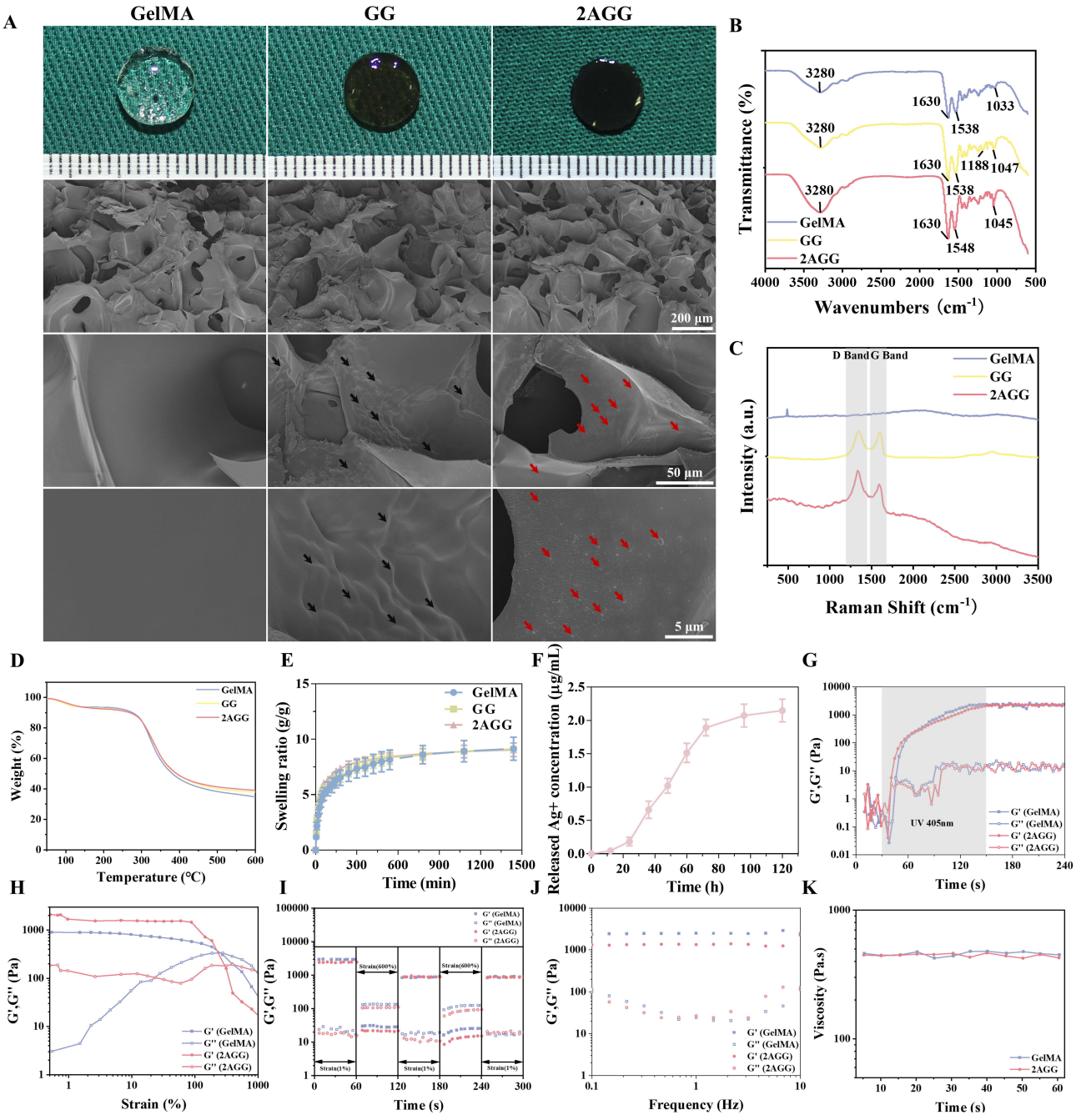

Figure 3 Characterization of prepared hydrogels. (**A**) Digital images and SEM images of prepared hydrogels (The black arrow refers to GO NPs and red arrow refers to Ag/GO NPs, and scale bar = 200 μm, 50 μm, 5 μm, respectively). (**B**) FTIR spectra of GelMA, GG, and 2AGG hydrogels. (**C**) Raman spectra of GelMA, GG, and 2AGG hydrogels. (**D**) TGA results of GelMA, GG, and 2AGG hydrogels. (**E**) Swelling ratios of GelMA, and 2AGG hydrogels. (**F**) Ag^+ release profile of Ag/GO-GelMA hydrogel (n = 3). (**G**) Dynamic rheological observations of the crosslinking processes of 2AGG hydrogels. H–K) Rheological performance: (**H**) strain sweep, (**I**) dynamic step–strain, (**J**) frequency sweep, and (**K**) viscosity measurements of GelMA and 2AGG hydrogels, respectively.

The structural characteristics of Ag/GO-GelMA (2AGG) hydrogels were initially examined using SEM. As depicted in Figure 3A and Figure S2A, the three-dimensional porous structure of the hydrogels was clearly visible. It is worth noting that the surface of the pristine GelMA hydrogel was very smooth. Upon incorporation of Ag/GO, the hybrid hydrogel predominantly exhibited a rough surface, and higher magnification confirmed the uniform distribution of Ag/GO nanoparticles within the hydrogel. In addition, there was no significant difference in the mean pore size of the three hydrogels (Figure S3). Then, the chemical structure of the resulting hydrogels was determined using Fourier transform infrared (FTIR) spectroscopy (Figure 3B). The pure GelMA hydrogel and the hybrid GelMA hydrogel all exhibited absorption peaks corresponding to O–H, C=O, and C=C twisting vibrations at approximately 3280, 1630, 1538, and 1033 cm^{-1}.[32] Notably, upon the introduction of GO nanoparticles, a redshift was observed in the hybrid GG hydrogel, with the characteristic peak of GO appearing at 1188 cm^{-1},[23] while the twisting vibration peak shifted from 1033 cm^{-1} to 1047 cm^{-1}. Moreover, following the introduction of Ag/GO nanoparticles, the hybrid 2AGG hydrogel exhibited a redshift phenomenon, with the respective peaks shifting from 1033 cm^{-1} and 1538 cm^{-1} to 1045 cm^{-1} and 1548 cm^{-1}. This alteration can be attributed to the partial disruption of hydrogen bonds within the GelMA hydrogel network, caused by the emergence of novel interactions, such as electrostatic forces, between the hydrogel and Ag/GO. Consequently, this observation indirectly validates the effective integration of Ag/GO nanoparticles into the GelMA matrix. Furthermore, the Raman spectra analysis reveals the presence of distinct D and G peaks at approximately 1338cm^{-1} and 1597cm^{-1}, respectively,[33] subsequent to the incorporation of GO and Ag/GO nanoparticles. These peaks are recognized as characteristic signatures of carbon atoms. This observation serves as evidence for the successful synthesis of the Ag/GO-GelMA hydrogel, as depicted in Figure 3C and Figure S2B. Following that, an investigation was conducted on the thermal stability of the hydrogel, as depicted in Figure 3D and Figure S2C. It was observed that the residual weight of the 2AGG hydrogel at a temperature of 600 °C was marginally greater than that of the pure GelMA hydrogel and the GG hydrogel. This observation suggests that the presence of Ag/GO NPs enhances the thermal stability of the hybrid hydrogel. Afterward, an investigation was conducted to determine the dynamic swelling ratio of the hydrogels through immersion in PBS until reaching swelling equilibrium (Figure 3E). The obtained equilibrium swelling ratios for GelMA and 2AGG were 9.0 and 9.1, respectively, demonstrating no significant disparity. This suggests that the incorporation of Ag/GO nanoparticles did not diminish the swelling characteristics inherent to GelMA. In addition, the quantification of Ag ions release by the Ag/GO NPs and Ag/GO-GelMA hydrogel was conducted and depicted in Figure 3F and Figure S4. At the 12th hour, Ag/GO NPs released 1.41 μg mL^{-1} of Ag ions, which reached about 70% of the total concentration of Ag ions in solution, while Ag/GO-GelMA hydrogel released only 0.05 μg mL^{-1} of Ag ions, indicating that Ag/GO-GelMA hydrogel could significantly slow down the release of Ag ions. The findings revealed that the GelMA matrix exhibited a gradual release characteristic towards Ag ions, thereby mitigating their oxidation and extending their antibacterial efficacy.

Hydrogels utilized as wound dressings necessitate tailored mechanical characteristics to cater to diverse wound types, such as irregular and deep wounds. Notably, hydrogel dressings exhibit inherent self-healing capabilities that effectively address the pressure exerted at wound sites due to bodily movements, thereby enhancing their safety and extending their longevity. At the same time, GelMA hydrogel possesses distinctive mechanical attributes of its own. In this study, a comprehensive examination was conducted of the mechanical characteristics of synthesized hydrogels.[21] The variations in shear storage moduli (G′) and shear loss moduli (G″) were meticulously monitored over time. G′ was utilized to assess the solid attributes, whereas G″ was employed to evaluate the fluid attributes of the hydrogels.[34] First, the rheological test evaluating GelMA/2AGG hydrogel's photosensitive behavior (indicated by gray labeling during the photo-crosslinking process starting at 30s) demonstrated that GelMA and 2AGG hydrogel could rapidly crosslink within a relatively short and safe exposure time (90–120s) in Figure 3G. However, the gradients of the G' curves in the anterior regions also serve as indicators of the crosslinking velocities of hydrogels. A steeper gradient implies a larger alteration per unit of time, thereby signifying a more rapid crosslinking rate.[35] Figure 3G reveals that the gradient of the G' curve in the anterior region of 2AGG is marginally lower than that of GelMA, potentially attributable to the incorporation of Ag/GO nanoparticles, which induces a transition of the hydrogel from a transparent state to a black state, consequently diminishing the light transmission capacity of the hydrogel. Then, the strain sweep assay revealed that the hydrogel point of GelMA and Ag/GO-GelMA (2AGG) was approximately 300% (Figure 3H). Subsequently, a dynamic step-strain

rheological experiment was conducted to quantitatively evaluate the self-healing ability of the engineered hydrogels (Figure 3I). An initial rheological recovery test was conducted to assess the Ag/GO-GelMA hydrogel by quantifying the storage modulus (G′) and the loss modulus (G″). A small strain of 1% was selected, while a large strain of 600% (Exceeding twice the tipping point) was maintained. Based on the findings presented in Figure 3I, it was observed that the G′ value was inferior to G″ under the influence of a high strain (600%), indicating the occurrence of hydrogel collapse. Upon the applied dynamic strain reaching 1%, the G′ value exhibited a significant increase, surpassing G″, thereby signifying the restoration of the hydrogel state in the sample. It is noteworthy that this phase transition can be repeated even after three alternately cycles, demonstrating the certain self-healing capability of the Ag/GO-GelMA hydrogel.[36] Afterward, according to the findings presented in Figure 3J, the dynamic frequency sweep analysis revealed that the storage modulus (G′) consistently exceeded the loss modulus (G″) as the frequencies increased from 0.1 to 10 Hz. This observation suggests that the 2AGG hydrogel primarily exhibited elastic behavior. Further, the rheological viscosity test demonstrated that there was no significant disparity in viscosity between the 2AGG hydrogel and pure GelMA hydrogel (Figure 3K). Moreover, as depicted in Figure S2D, the 2AGG hydrogel exhibited the same shear thinning behavior as GelMA, wherein the viscosity decreased with an increase in shear rate.[37] Furthermore, compressive strain-stress curves are employed to assess the mechanical strength of the hydrogels, with the corresponding slopes of these curves being calculated to determine the elastic modulus (Figure S5). The results indicate that the compressive stress of the three hydrogels increases slightly within the 0–50% compressive strain range. However, at 50–60% compressive strain, the hydrogels collapse as the compressive stress escalates (Figure S5A). Concurrently, Figure S5B demonstrates that there is no significant difference in the elastic modulus among the three hydrogels. These findings collectively suggest that the incorporation of Ag/GO nanoparticles did not substantially modify the intrinsic mechanical characteristics of GelMA hydrogels.

Photothermal Performance of Ag/GO-GelMA Hydrogels In Vitro

As previously mentioned, the integration of Ag/GO nanoparticles into GelMA hydrogel was undertaken to mitigate the decline in photothermal efficacy resulting from nanomaterial aggregation. To substantiate this supposition, the photothermal conversion efficiency (η) of Ag/GO and Ag/GO-GelMA at a wavelength of 808 nm was initially evaluated. At an equivalent concentration of Ag/GO nanoparticles, the efficiency (η) of Ag/GO and Ag/GO-GelMA was determined to be 46.2% and 47.6% respectively (Figure S6). These values were notably higher than those reported for other systems, supporting our hypothesis that promoting the dispersion of Ag/GO NPs and preventing aggregation contributes to the enhancement of the photothermal performance in the hybrid hydrogels. Consequently, the Ag/GO-GelMA hydrogel was chosen as the model sample for subsequent photothermal ability assessments.

The photothermal capability of the GG hydrogel and Ag/GO-GelMA (1AGG, 2AGG, and 5AGG) hydrogel were initially examined at various power levels (Figure 4A and Figure S7A and B). Specifically, the temperature of the 2AGG hydrogel increased from 24.5 to 51.5 °C within 3 minutes and reached 58.4 °C within 5 minutes when exposed to an 808 nm NIR laser (0.5 W cm^{-2}). With increasing laser power, the temperature of the 2AGG hydrogel rose to 79.5 °C (1.0 W cm^{-2}) and 88.2 °C (1.5 W cm^{-2}) after 5 minutes of 808 nm NIR irradiation. As same as GG hydrogel, the 2AGG hydrogel demonstrated remarkable photothermal stability even after undergoing four cycles of on-off NIR laser irradiation, as evidenced by the absence of any significant decrease in the maximum heating temperature (Figure S7C and D). In comparison, the pure GO-modified hydrogel (GG) exhibited a comparatively weaker capacity for photothermal heating (Figure 4A). Specifically, when subjected to 1.0 W cm^{-2} 808 nm irradiation for a duration of 3 minutes, the central temperature of the 2AGG gel reached 66.6 °C, whereas the GG hydrogel only reached a temperature of 52.4 °C. The findings of this study indicate that the Ag/GO-GelMA hydrogel that was designed exhibited remarkable photothermal capabilities, suggesting its potential as a photothermal platform for antibacterial therapy. However, since the effective temperature of photothermal therapy is above 42 °C,[38] and the temperature threshold of human skin scald is about 60 °C,[39] we chose 2AGG hydrogel to irradiate at 808nm NIR of 0.5 W cm^{-2} for 3 minutes (51.5 °C) for the following antibacterial experiment.

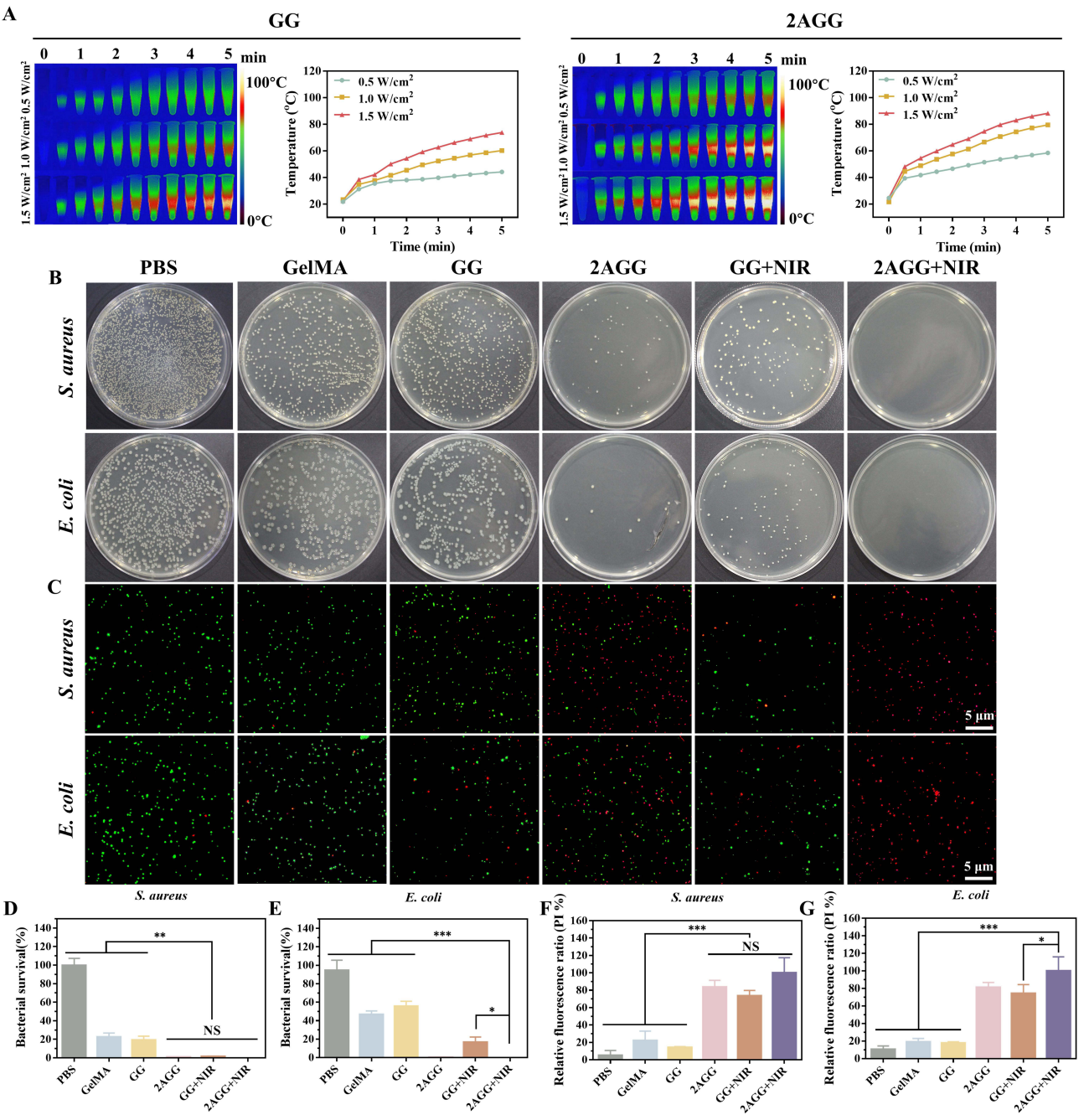

Figure 4 Photothermal and antibacterial performance in vitro. Photothermal properties of Ag/GO-GelMA (2AGG) hydrogel: (**A**) infrared thermal images and photothermal temperature rise curves under 808 nm NIR irradiation with different laser power densities (0.5, 1.0, and 1.5 W cm^{-2}) of GG and 2AGG; Antibacterial ability of hydrogels: (**B**) colonization, (**C**) confocal fluorescence, (**D**), (**E**) antibacterial rates and (**F**), (**G**) relative fluorescence ratios of *S. aureus* and *E. coli* after treatments with PBS, GelMA, GG, 2AGG, GG + NIR, and 2AGG + NIR (n = 3).

Notes: * Indicates significant difference (* P < 0.05, ** P < 0.01, *** P < 0.001) and NS means not significant.

Photothermal Antibacterial Property of Ag/GO-GelMA Hydrogels In Vitro

The remarkable photothermal conversion efficiency exhibited by the Ag/GO-GelMA hydrogel in its original state serves as a catalyst for our investigation into its potential antibacterial properties. In this study, we examine the in vitro antibacterial efficacy of the Ag/GO-GelMA hydrogel against two prevalent bacterial strains, namely the Gram-negative *E. coli* and the Gram-positive *S. aureus* (Figure 4B and C), which are commonly associated with a multitude of infectious diseases. According to the data shown in Figure 4B–E, the presence of Ag-containing nanoparticles in the Ag/GO-

GelMA system demonstrated a significant antibacterial effect, attributed to the sustained release of Ag ions.[15] This was evidenced by the enhanced bactericidal ability of the 2AGG hydrogel compared to the GG hydrogel, which contained GO without Ag modification. The 2AGG hydrogel exhibited the ability to eliminate 99.2% of *S. aureus* and 99.6% of *E. coli*. Furthermore, after NIR irradiation, the temperature of the bacterial suspension containing 2AGG exhibited a substantial increase, rising from 37 to 59.6 °C (Figure S8). Notably, upon NIR irradiation, the 2AGG hydrogel, in conjunction with an 808 nm NIR laser (0.5 W cm^{-2}, 3 min), effectively inactivated almost all *S. aureus* (99.9%) and *E. coli* (99.9%). Conversely, the bacterial solution containing GG experienced a minimal temperature rise, reaching only 44.3 °C under the same duration and power of NIR irradiation. Additionally, the GG hydrogel displayed a bactericidal efficacy of 98.5% against *S. aureus* and 83.3% against *E. coli*, as depicted in Figure 4D and E. In some previous studies, when they used PHTAs for PTT, they often required higher laser power and longer laser irradiation time. For example, Chen et al employed PTT to enhance the healing of diabetic wounds, necessitating a laser power of 1.5 W cm^{-2} and an irradiation duration of 5 minutes.[17] Similarly, Yan et al applied PTT to facilitate the healing of infectious wounds, requiring a laser power of 2.0 W cm^{-2} and an irradiation time of 5 minutes.[18] Furthermore, Qi et al developed a stable multifunctional agarose/polydopamine/ε-PL hydrogel (ADPH) wound Dressing, which necessitates up to 10 minutes of near-infrared laser irradiation for PTT of the infectious wound.[31] Compared with them, the Ag/GO-GelMA hydrogel only needs lower near-infrared (NIR) laser power and shorter irradiation durations to achieve a superior antibacterial effect. These findings indicate that the Ag/GO-GelMA platform, combining Ag/GO nanoparticles for Ag ions release and photothermal sterilization, exhibited a considerably enhanced photothermal conversion efficiency and potent antibacterial activity.

In order to investigate the antibacterial properties of the Ag/GO-GelMA (2AGG) hydrogel, a live/dead staining assay using SYTO9/PI was conducted. SYTO9 staining resulted in green fluorescence for live bacteria, while dead bacteria were identified through PI labeling and emitted red fluorescence. Figure 4C illustrates that *S. aureus* and *E. coli* treated with PBS exhibited significant green fluorescence, with only a small number of bacteria displaying red fluorescence.[40] In contrast, the GelMA hydrogel and GG hydrogel treatment groups exhibited more red fluorescence than the PBS group. Furthermore, the intensity of the red color increased gradually in the Ag/GO doped GelMA hydrogel, and the 2AGG + NIR treatment group demonstrated the most pronounced red fluorescence, indicating a synergetic eradication effect on *S. aureus* and *E. coli*. Moreover, the red fluorescence observed in the GO-loaded hydrogel (GG) was considerably lower compared to the GelMA hydrogel loaded with Ag/GO nanoparticles upon illumination (2AGG). This phenomenon can be attributed to the comparatively weaker photothermal properties (43.3 °C, Figure S8) and lower photothermal conversion efficiency of GG hydrogel in comparison to 2AGG, which ultimately hindered its ability to effectively eliminate bacteria. It is noteworthy that both the plate counting assay and fluorescence-based assessment yielded consistent antibacterial trends (Figure 4D–G), thereby providing additional evidence to support the promising prospects of Ag/GO-GelMA hydrogel in facilitating efficient antibacterial therapy through the synergistic interaction between the hydrogel and photothermal therapy. The findings of this study provide confirmation that the antibacterial platform (2AGG + NIR) exhibited a significant bactericidal effect through PTT with high PCE and sustained release of Ag^{+}.

Biocompatibility and Migration Evaluation In Vitro

The biocompatibility of a hydrogel is of utmost importance for its in vivo antibacterial application.[41] Prior to conducting in vivo experiments, the cytocompatibility of the hydrogels produced in their current state was investigated using the live/dead cell staining technique. Figure 5A demonstrates that similar to the control group, no discernible red fluorescence was detected when HaCAT cells were co-incubated with the hydrogels. Additionally, the hydrogel treatments did not have any impact on cell growth and proliferation, as indicated in Figure 5B. Then, the cytotoxicity of the hydrogels towards HaCAT cells was evaluated using the CCK-8 assay. In comparison to the control group, the hydrogels exhibited no notable cytotoxic effects on HaCAT cells after 1, 3, and 5 days of coculture, as depicted in Figure 5C. These findings suggest that the hydrogels are non-toxic. Consequently, the GelMA-based hydrogels, which possess ascendant biocompatibility, are well-suited for in vivo anti-infective therapy.

Subsequently, we conducted an assessment of the impact of hydrogel on cell migration, given that cell migration serves as the initial and indispensable stage in tissue regeneration.[42] Specifically, GelMA-based hydrogels (GelMA, GG,

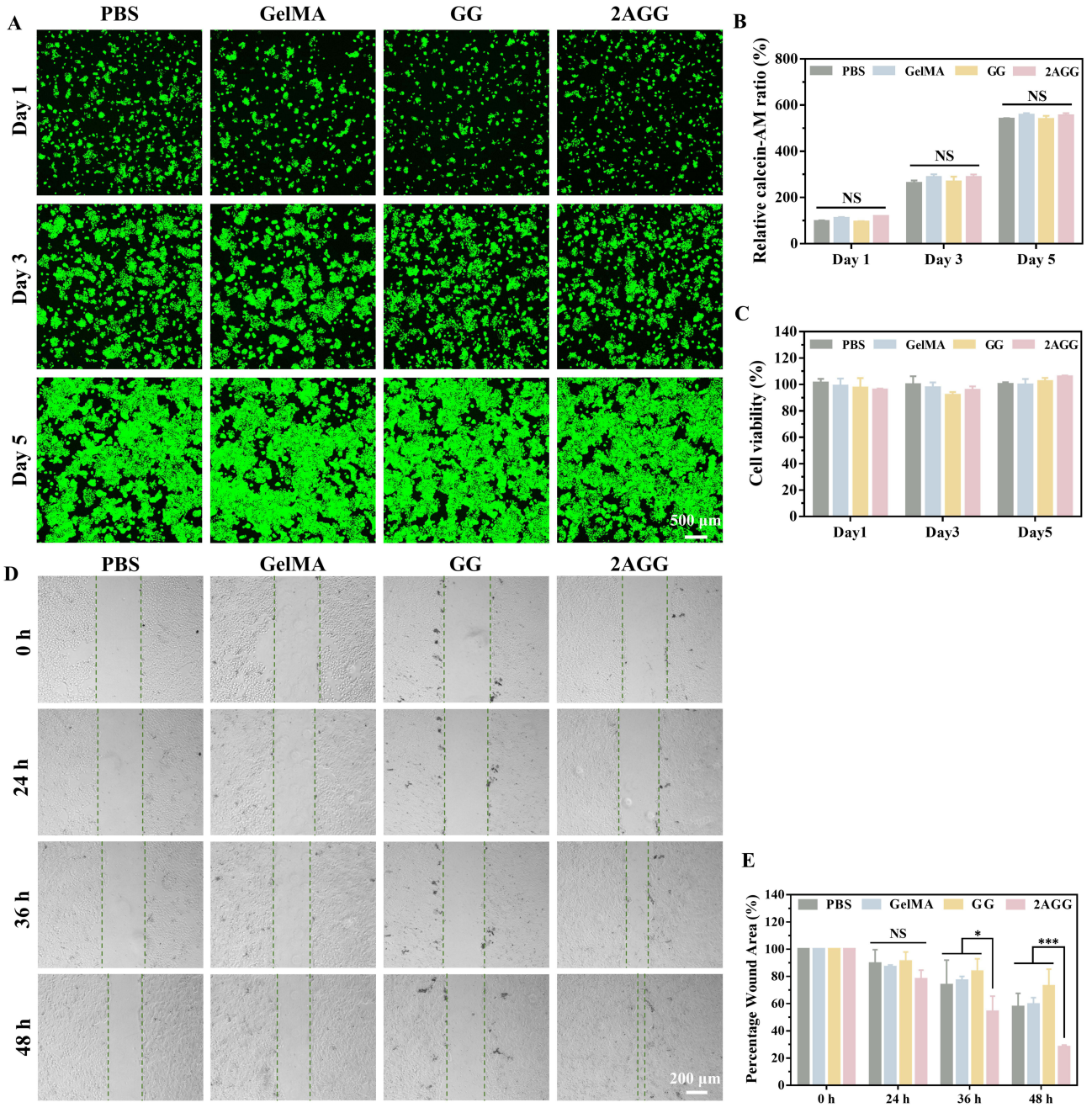

Figure 5 In vitro biocompatibility and migration evaluation. Biocompatibility of prepared hydrogels: (**A**) Fluorescent images and (**B**) Relative calcein-AM fluorescence ratio of calcein-AM and PI double-stained HaCATs cells after treating with different samples for 1 day, 3 days, and 5 days (n = 3). NS means not significant. (**C**) CCK-8 analysis of HaCATs after treatments with the negative control (PBS) and hydrogel samples (GelMA, GG, and 2AGG) for 1 day, 3 days, and 5 days (n = 3). Migration evaluation of Ag/GO-GelMA hydrogel: (**D**) HaCATs cells migration images after being treated with prepared hydrogels. (**E**) The corresponding wound area changes after being treated with PBS, GelMA, GG, and 2AGG. Scale bar = 200 μm. (n = 3).

Notes: * Indicates significant difference (* $P < 0.05$, *** $P < 0.001$) and NS means not significant.

and 2AGG) were administered to HaCAT cells for the purpose of conducting a wound scratch examination. The results depicted in Figure 5D and E demonstrated that, following a co-incubation period of 24, 36, and 48 hours, the cells treated with 2AGG hydrogel exhibited a significantly accelerated migration rate compared to the control group. After 36 hours, the proportion of remaining wounds in the 2AGG hydrogel group and the control group were approximately 54.2% and 73.6%, respectively. After 48 hours, the wound in the 2AGG hydrogel group exhibited significant healing (28%), whereas the wound region in the control group remained at a high level of 57.4%. This observation implies that the

presence of Ag NPs facilitates cell migration. Kurain et al previously documented that GelMA hydrogel encapsulating Ag NPs effectively enhances cell migration without inducing noticeable toxicity.[43] Similarly, Cao et al conducted a separate study, which further confirmed that appropriate concentrations of Ag NPs greatly stimulate cell migration.[44] However, in the group treated with GG hydrogel, the remaining wound area still reached 72.7% after 48 hours of incubation, potentially attributable to the cytotoxicity exhibited by the aggregated GO NPs.[45] With the incorporation of Ag NPs into the GO NPs, the aggregation of GO NPs was significantly alleviated, therefore reducing the cytotoxicity and significantly decreasing the wound area to 28% in the 2AGG group.[15] These results demonstrate that the 2AGG hydrogel exhibits excellent biocompatibility and significantly enhances cell migration, thereby promoting wound healing.

Infected Wound Healing Evaluation and Antibacterial Assay In Vivo

The antibacterial efficacy of the 2AGG hydrogel was evaluated in vivo using a rat model infected with *S. aureus* (Figure 6A). The photothermal performance of the hydrogel was initially assessed using an infrared camera after application onto the rat's back skin wounds. Figure 6B and C demonstrates that, following 3 minutes of 808 nm NIR irradiation at a power density of 0.5 W cm^{-2}, the temperature of the wound region increased to 57.8 °C for the 2AGG hydrogel. In contrast, the temperature of the hydrogels lacking Ag/GO nanoparticles, GelMA and GG, only reached 31.1 °C and 49.3 °C, respectively, under the same conditions. Following various treatments, the presence of bacteria at the wound sites was assessed using the agar plate method to assess the bactericidal efficacy on day 3 (Figure 6D and E). Evidently, a substantial quantity of bacteria was observed on the agar plates of the control group, with a gradual decrease in bacterial count observed upon the application of hydrogel and NIR treatments. Notably, the 2AGG + NIR group exhibited a significant reduction in bacterial growth on the agar plate, consistent with the in vitro findings. These results offered intuitive proof that the 2AGG hydrogel with improved photothermal conversion efficiency by Ag/GO NPs could serve as a robust platform for antibacterial treatment both in vitro and in vivo.

Moreover, the wound healing progression in rats subjected to various treatments (PBS, GelMA, GG, 2AGG, GG + NIR, and 2AGG + NIR) was visually assessed through photographic documentation (Figure 6F–H). The corresponding schematic depictions of wound contraction and the subsequent calculation of wound contraction were provided in Figure 6F and H, respectively. In all groups that were tested, the size of the wound exhibited a gradual decrease over time. Specifically, on day 12, the wound that was treated with 2AGG + NIR displayed the smallest open wound area (5.7%), accompanied by the development of smooth epidermal and dermal tissues. In contrast, the GG + NIR, 2AGG, GG, GelMA, and PBS groups exhibited open wound areas of 16.9%, 15.9%, 19.1%, 18.7%, and 23.2%, respectively, along with noticeable uneven scar tissues. The findings of this study indicate that the group treated with 2AGG + NIR exhibited superior efficacy in wound healing compared to the other groups. This can be attributed to the combined effect of NIR-assisted photothermal ablation of bacteria (mainly due to the Ag/GO-mediated photothermal antibacterial property, especially after the decoration of Ag NPs on GO NPs to improve the photothermal conversion efficiency) and the inherent antibacterial properties of the hydrogel, which synergistically enhanced the antibacterial activity of the developed platform. Consequently, this platform effectively eradicates pathogens and expedites the wound-healing process.

To validate the aforementioned therapeutic outcomes, the assessment of wound healing was conducted through the examination of histological alterations in skin tissues. Following the treatments, rats were sacrificed at predetermined intervals, and skin tissues from the PBS, GelMA, GG, 2AGG, GG + NIR, and 2AGG + NIR groups were collected. These skin tissues were stained with hematoxylin and eosin (H&E) (Figure 7A, B and Figure S9), Masson (Figure 7C and D), IL-6 (Figure 7E), and CD31 (Figure 7F). The results of the H&E staining demonstrated that on day 12, the scar width of the group treated with 2AGG + NIR (0.66 mm) was significantly smaller compared to the groups treated with PBS (3.75 mm), GelMA (2.47 mm), GG (2.94 mm), 2AGG (1.96 mm), and GG + NIR (2.16 mm) (Figure 7A and B). Simultaneously, H&E images of higher magnification revealed that the control group exhibited a severe inflammatory response on days 7 and 12.[46] In contrast, the 2AGG + NIR group did not exhibit noticeable inflammation(Figure 7B, Figure S9A and B). Furthermore, the 2AGG + NIR group displayed the presence of regenerated dermis tissue containing appendages such as hair follicles. In addition, a substantial generation of micro-vessels and capillaries was observed, indicating a significantly higher level of angiogenesis compared to the other groups (Figure 7B, Figure S9A and C).

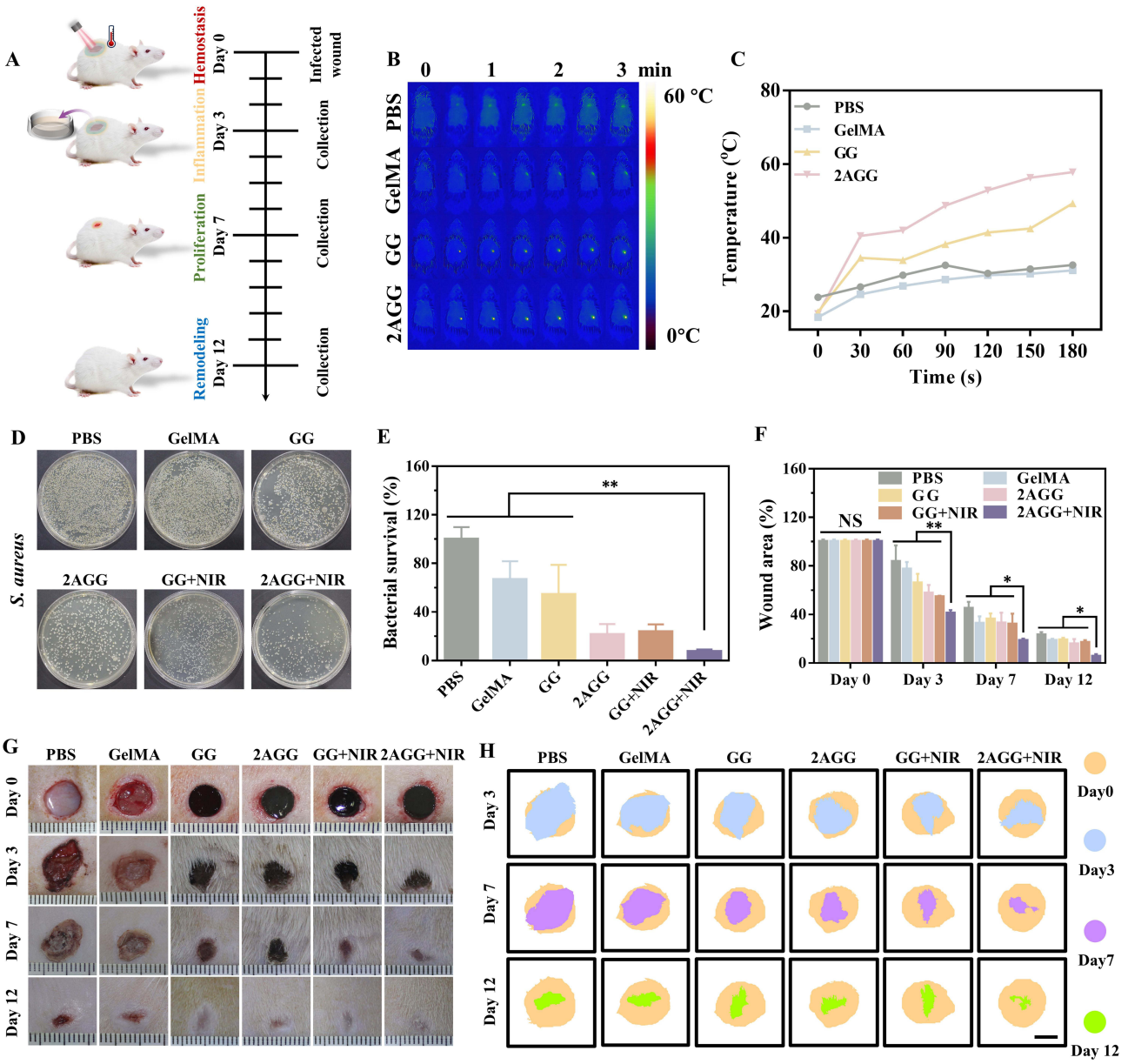

Figure 6 In vivo assessment of the NIR light-induced antibacterial properties of Ag/GO-GelMA hydrogel. (**A**) Schematic illustration of the timeline of *S. aureus*-infected wound model development and photographs or tissue collection. (**B**) Infrared thermal images and (**C**) corresponding temperature advancement at the wound sites of rats in the PBS and hydrogels groups at determined times under 808 nm NIR irradiation (0.5 W cm^{-2}). (**D**) Photographs and (**E**) quantitative analysis of bacterial colonies on agar plates from wound sites on day 3 (n = 3). (**F**) wound area (n = 3), (**G**) Photographs of infected wounds, and (**H**) schematic images of wound contraction treated with different samples from day 0 to 12 (n = 3).

Notes: * Indicates significant difference (* $P < 0.05$, ** $P < 0.01$) and NS means not significant.

Moreover, the 2AGG + NIR group exhibited a conspicuous presence of continuous, regular, and closely intertwined collagen fibers, whereas the collagen fibers in the remaining groups displayed a lesser degree of organization and looser arrangement (Figure 7C and D). Afterward, the results obtained from immunofluorescence staining using DAPI and IL-6 demonstrated a significant decrease in the expression of the inflammation marker IL-6 in the wound area of the 2AGG + NIR group compared to the other five groups (Figure 7E).[47] Additionally, the NIR-assisted 2AGG hydrogel exhibited the highest expression of CD31 compared to the other groups that were tested (Figure 7F).[48] The wound width (Figure 7G), collagen deposition amounts (Figure 7H), IL-6 (Figure 7I) and CD31 (Figure 7J) were quantitatively analyzed respectively, and the results were consistent with the observed phenomena in the Figure 7A–F. These findings align with the results obtained from H&E staining on day 7, indicating that the combination of 2AGG and NIR possesses remarkable

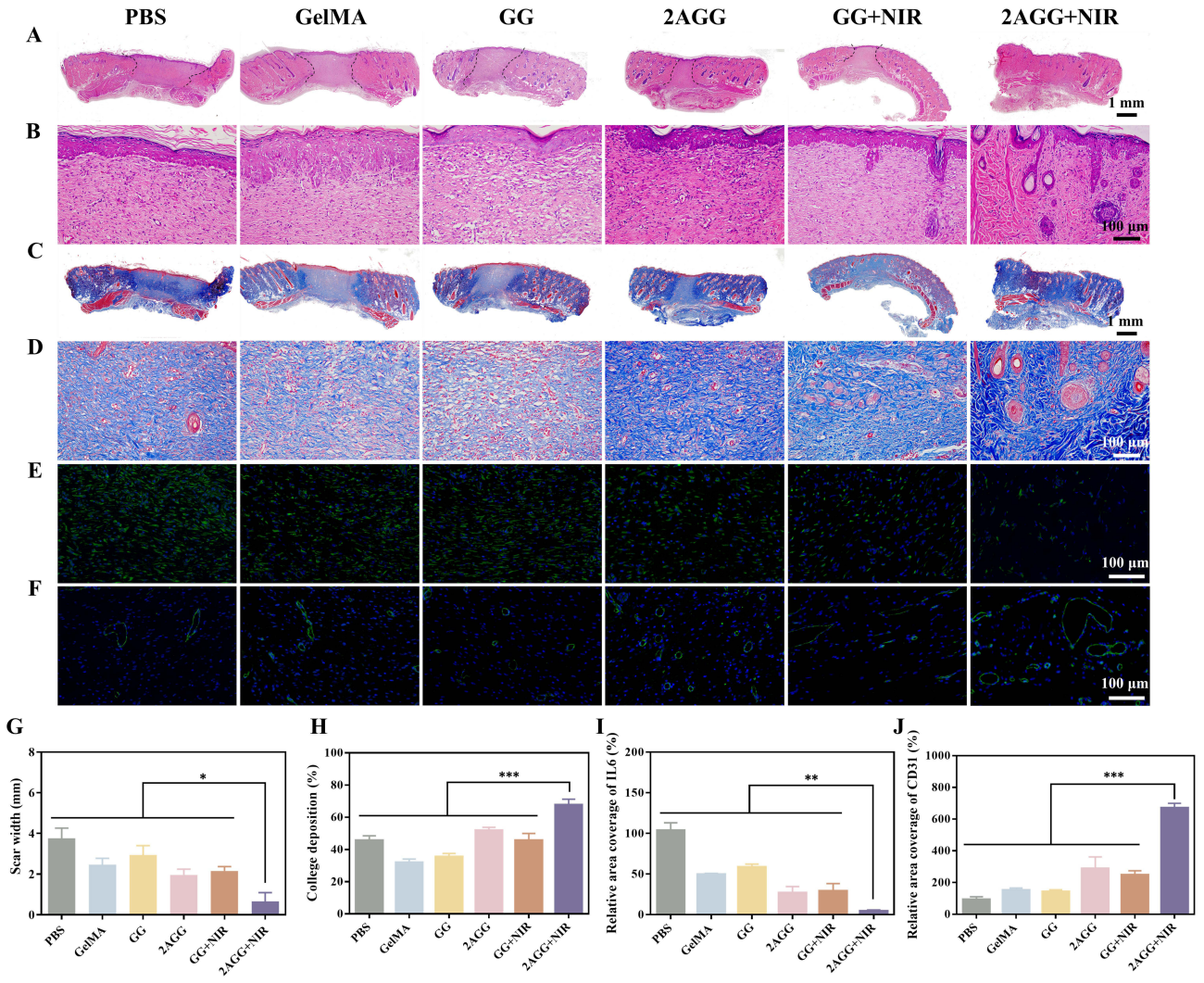

Figure 7 Changes in histological characteristics after skin tissue has been healed with various formulas. (**A**), (**B**) H&E staining, (**C**), (**D**) Masson's staining, (**E**) IL-6 staining, and (**F**) CD 31 staining of the skin tissues from the wound boundaries on day 12. G–J) Quantitative analysis of stained images attained from different groups: scar width, college deposition, IL-6, and CD 31, respectively (n = 3).
Notes: * Indicates significant difference (* $P < 0.05$, ** $P < 0.01$, and *** $P < 0.001$).

anti-inflammatory properties and promotes angiogenesis effectively. Significantly, in comparison to the GG hydrogel, incorporating pure GO nanoparticles into GelMA hydrogel without Ag deposition, the 2AGG hydrogel containing Ag-modified GO nanoparticles demonstrated a greater photothermal heating capacity (>50 °C) utilizing NIR, thereby effectively eradicating bacteria and expediting the transition from the inflammatory to the reparative phase of the wound: antibacterial action by PTT with high PCE and Ag^+ sustained release during the inflammatory phase of wound healing, and promoting angiogenesis and collagen deposition during the proliferative phase. These findings substantiate the potential of the Ag/GO-GelMA hydrogel as a promising platform for in vivo antibacterial therapy and wound healing.

Wound Healing Mechanisms of the Ag/GO-GelMA Hydrogels

To investigate the underlying effects of the Ag/GO-GelMA hydrogel, we conducted RNA sequencing analysis on wound tissues obtained from infected rats on day 12 following hydrogel treatment. A total of 32,624 genes were found to be co-expressed in tissues from experimental groups. Among these, approximately 20,817 genes exhibited differential expression between the control (PBS) group and the 2AGG + NIR groups, while approximately 285 genes showed differential expression with a $|\log_2 FC| \geq 1$ and p-value ≤ 0.05. In Figure 8A, we utilized GeneCard and OMIM-Gene-Map-Retrieval to retrieve 1612

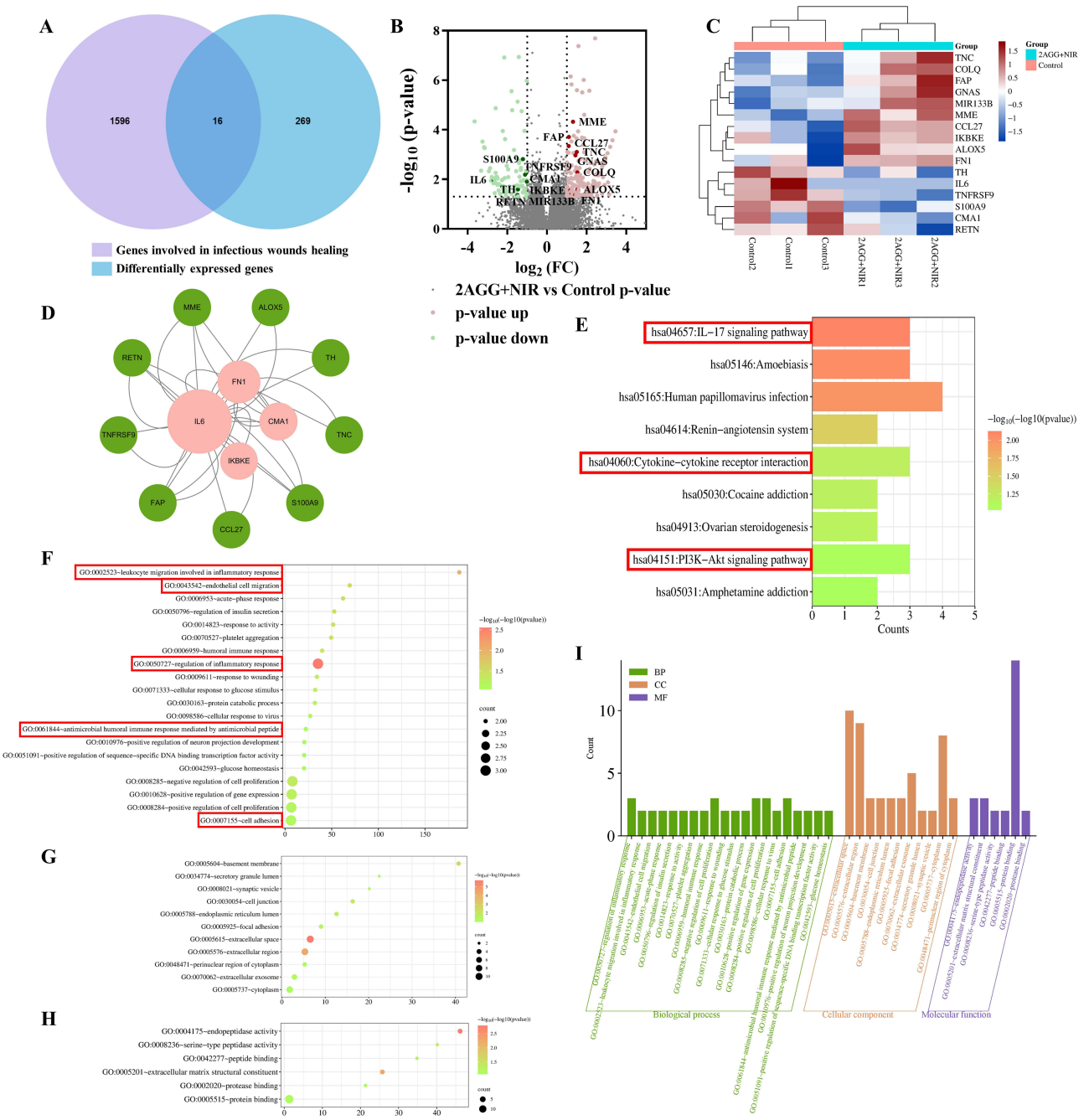

Figure 8 Therapeutic mechanisms of Ag/GO-GelMA (2AGG) hydrogel in wound healing. (**A**) Venn diagram of the transcriptomic profiles between differentially expressed genes ($|\log_2 FC| \geq 1$ and p-value ≤0.05) and genes involved in infectious wound healing. (**B**) the volcano plot and (**C**) heatmaps of the differentially expressed genes (DEGs) of significantly changed genes after 2AGG + NIR treatment ($|\log_2 FC| \geq 1$ and p-value ≤0.05). (**D**) Protein–protein interaction (PPI) network, (**E**) The KEGG pathway enrichment analysis, (**F**) biological process, (**G**) cellular component, (**H**) molecular function, and (**I**) the GO enrichment analysis of the 16 intersection genes.

genes associated with the healing process of infectious wounds. These genes were intersected with differentially expressed genes with $|\log_2 FC| \geq 1$ and p-value ≤0.05 (DEGs) between the two groups to obtain 16 intersection genes. Figure 8B and 8C display the volcano plot and heatmaps of the intersection genes. The intersection genes were further examined through protein-protein interaction (PPI) network analysis. The color intensity and size of each node in the PPI network indicate the strength of their association with other protein molecules, ranging from green to red. Figure 8D demonstrates that the PPI analysis identified key signaling molecules involved in inflammation regulation and cell migration promotion, including IL-6, FN1, IKBKE, TNC, and S100A9.[49–52] Kyoto Encyclopedia of Genes and Genomes (KEGG) pathway enrichment analysis of

the 16 intersection genes (Figure 8E) showed that those genes were significantly enriched in IL-17 signaling pathway, indicating that the combined treatment of 2AGG + NIR may facilitate the healing of infectious wounds by down-regulating IL-6 and S100A9 and up-regulating IKBKE to inhibit the activation of IL-17 signaling pathway downstream of MAPK signaling pathway.[53,54] Furthermore, it is noteworthy that certain genes exhibited enrichment in additional signaling pathways, namely the PI3K-Akt signaling pathway and Cytokine-cytokine receptor interaction. This observation serves as a reminder that the combination of 2AGG + NIR may potentially reduce inflammatory response, and promote angiogenesis, cell migration, and proliferation through the PI3K-Akt signaling pathway and Cytokine-cytokine receptor interaction.[55–58] Subsequently, a Gene Ontology (GO) enrichment analysis was conducted (Figure 8F–I). The analysis revealed several significantly enriched biological processes, including regulation of inflammatory response, leukocyte migration involved in inflammatory response, antibacterial humoral immune response mediated by antibacterial peptide, endothelial cell migration, and cell adhesion. The findings depicted in Figure 5D, E, and Figure 7E, I demonstrate that following treatment with 2AGG + NIR, there was an increase in cell migration rate and a decrease in the positive rate of IL-6 immunofluorescence staining, which aligns with the transcriptome data.

The findings from RNA sequencing analysis revealed that the application of 2AGG hydrogel combined with NIR to wounds exhibited dual benefits of promoting tissue repair and regeneration, while concurrently downregulating the expression of inflammation-associated genes, particularly IL-6. Additionally, the discovery of associated genes and pathways accountable for the expedited wound healing mechanism holds the potential for their utilization as a significant framework in the formulation and advancement of innovative therapeutic approaches.

Hemolysis and Biocompatibility Evaluation In Vivo

The hydrogel at the wound interface performs various functions such as hemostasis, exudate adsorption, acting as a barrier to microorganisms, facilitating gaseous exchange, and providing a scaffold for cells, which can potentially contribute to the promotion of wound healing.[59] To evaluate the hemostatic performance in vivo, the rat tail amputation model (Figure 9A and B) was employed. Following a 15-second tail-cutting procedure, GelMA-based hydrogels (GelMA, GG, and 2AGG), a positive control group (gauze), and a negative control group (phosphate buffered saline, PBS) were applied to the wound. The blood loss observed in the negative control groups (PBS group) was notably higher compared to the other groups, with a recorded value of 125.0 ± 27.5 mg of blood. In contrast, the GelMA-based groups exhibited a significant reduction in blood loss, with no significant difference observed when compared to the positive control group (gauze). This substantial decrease in blood loss indicates that the GelMA-based hydrogels (GelMA, GG, and 2AGG) we synthesized possess effective capabilities in achieving hemorrhage control, thereby facilitating the process of wound healing.

The in vivo biocompatibility of the 2AGG hydrogel was assessed, followed by the collection of blood samples and main organs from rats in each group on day 12 post-treatment for subsequent analysis (Figure 9). A hemolysis assay was conducted to evaluate the hemocompatibility of the 2AGG hydrogel. The positive control group, treated with Triton X-100, exhibited a vivid red supernatant, indicating the occurrence of hemolysis. Conversely, the GelMA, GG, and 2AGG groups displayed a transparent supernatant similar to that of the negative control group (PBS), as depicted in Figure 9C and D. Furthermore, the quantitative assay depicted in Figure 9C revealed that the hemolysis ratios of the three experimental groups were all below the internationally accepted threshold of 5% for hydrogels (4.4%, 4.5%, and 4.5%, respectively).[60] This observation suggests that the 2AGG hydrogel exhibits satisfactory hemocompatibility. Furthermore, we conducted an investigation into the cytotoxicity of the 2AGG hydrogel using hematoxylin and eosin (H&E) staining on sections of vital organs, namely the heart, liver, spleen, lung, and kidney, as previously described. The analysis did not identify any evident damage or histological abnormalities in any of the experimental groups (Figure 9E). In addition, as shown in Figure 9F–O, blood analysis (RBC, WBC, ALT, AST, LDH, PLT, HGB, BUN, CRE, HCT) of rats at the end of treatment showed that there were no obvious abnormalities in various blood indexes of rats treated with PBS, GelMA, GG, 2AGG, GG + NIR, 2AGG + NIR, indicating that the prepared hydrogel had good biocompatibility. Despite some researchers' worry about the potential toxicity of GO NPs, the composite hydrogel employed in this research demonstrated favorable biocompatibility, devoid of any obvious toxic manifestations associated with GO, which may be due to: (1) the low concentration of GO NPs, which is much lower than the 25 mg mL^{-1} demonstrated by Wu et al[45] (2) Ag NPs in GO surface modification and the addition of GelMA hydrogel with superior biocompatibility, which can prevent its

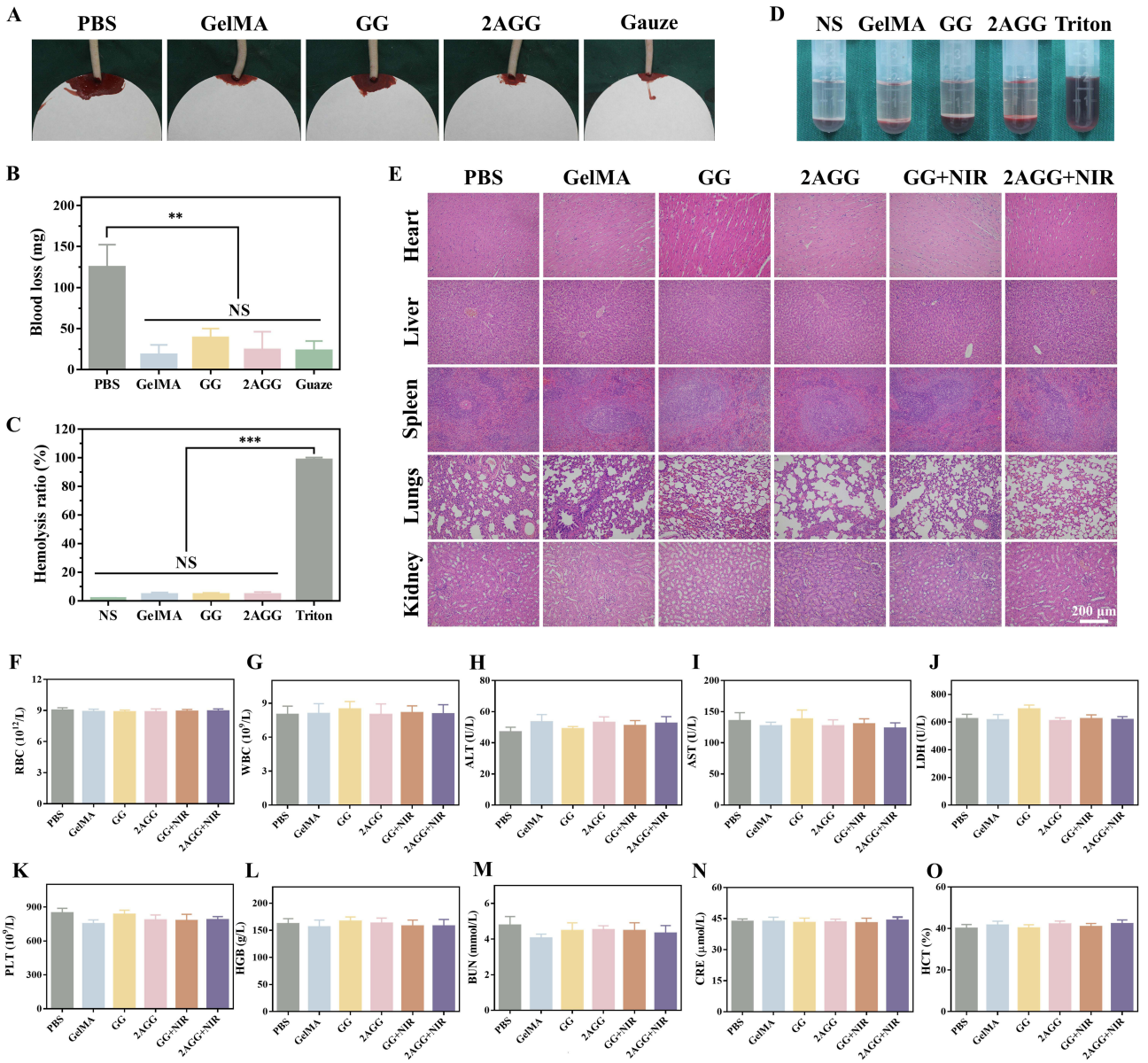

Figure 9 In vivo hemolysis and biocompatibility evaluation. (**A**) Representative images and (**B**) blood loss of PBS, GelMA, GG, 2AGG, and gauze in the rat-tail amputation model (n = 3). (**C**) hemolysis ratios of PBS, GelMA, GG, 2AGG, and Triton (n = 3) and (**D**) Photographs from the hemolysis test. (**E**) H&E staining of main organs (heart, liver, spleen, lung, and kidney) collected from rats in the different groups (Scale bar = 50 μm). F–O) Blood analysis of the rat at the end of treatment: (**F**) red blood cells (RBC), (**G**) white blood cells (WBC), (**H**) alanine transferase (ALT), (**I**) alanine transferase (ALT), (**J**) lactate dehydrogenase (LDH), (**K**) blood platelet (PLT), (**L**) hemoglobin (HGB), (**M**) blood urea nitrogen (BUN), (**N**) creatinine (CRE), (**O**) hematocrit (HCT).
Notes: * Indicates significant difference (** P < 0.01, and *** P < 0.001) and NS means not significant.

aggregation and greatly reduce its toxicity. (3) GO plays a role locally and does not enter the blood, but can be excreted from the body through lysosomes and immune cell phagocytosis.[61,62] These findings consistently confirm the remarkable biological safety of PTT facilitated by Ag/GO-loaded GelMA hydrogel, thereby highlighting the promising prospects of this methodology in clinical applications.

Material and Methods

Materials

Gelatin Methacryloyl (GelMA, GM-60) and Lithium Phenyl (2,4,6-trimethyl benzoyl) phosphinate (LAP) were purchased from EFL (Suzhou, China). Briefly, it was acquired through a process involving the alkali treatment of porcine

skin to obtain gelatin. Subsequently, the gelatin was subjected to a reaction with methacrylic anhydride (MAA) at a feed ratio of 0.035:1 (mL of MAA to g of gelatin), resulting in a 60% MAA substitution degree. This reaction took place at a temperature of 50 °C and a pH range of 8.5–9 for a duration of 180 minutes. The grafting of unsaturated bonds onto gelatin was achieved by converting the anhydride to an amino and hydroxyl group through a straightforward one-step reaction. Graphene oxide (GO) was acquired from XFNANO Material Tech Co., Ltd. Silver nitrate was procured from Alfa Aesar (Shanghai, China). Ammonium hydroxide (30 w v^{-1} % in water), Anhydrous Glucose, and anhydrous ethanol were obtained from Aladdin (Shanghai, China). The LIVE/DEAD™ BacLight™ Bacterial Viability Kit, which includes propidium iodide (PI) and SYTO9, was purchased from Thermo Fisher Scientific (L7012, Waltham, USA). The following reagents were procured from Beyotime Biotechnology (Shanghai, China): Human keratinocytes cells (HaCAT), Dulbecco's modified Eagle medium (DMEM), fetal bovine serum (FBS), Calcein-AM/PI Cell Viability Kit, penicillin-streptomycin (P/S), trypsin, Cell Counting Kit-8 (CCK-8), Triton X-100, and phosphate-buffered saline (PBS, pH = 7.4). These reagents were utilized in their original form without undergoing any additional purification or modification.

Fabrication of GO and Ag/GO Nanoparticles

In this study, GO nanoparticles were synthesized using a modified version of our previously reported method.[15] To elaborate, 60 mg of GO powder was dissolved in 20 mL of deionized water with the assistance of ultrasonication, followed by gentle stirring for a duration of 6 hours. The resulting GO nanoparticles were collected through high-speed centrifugation at 12,000 rpm for 10 minutes and subsequently washed three times with deionized water and anhydrous ethanol. Finally, the synthesized GO nanoparticles were freeze-dried and stored in a refrigerator at a temperature of 4°C for future utilization. Subsequently, Ag/GO nanoparticles were synthesized via a reduction-deposition procedure. Initially, 500 mg of $AgNO_3$ was dissolved in deionized water. Subsequently, ammonia solution was gradually introduced to the aforementioned solution until the brown precipitate dissolved and the solution regained clarity. Following this, GO nanoparticles (50 mL, 1 mg mL^{-1}) were incorporated into the solution, and the silver ions were reduced using a glucose solution (50 mL, 20 mg mL^{-1}). The resulting mixture was gently stirred at a temperature of 95 °C to deposit the glucose-reduced Ag nanoparticles on the GO nanoparticles surface, which was then centrifuged at 12,000rpm and washed with deionized water three times to further remove the excess glucose and finally produced Ag-decorated GO (Ag/GO) nanoparticles. Similarly, the prepared Ag/GO nanoparticles were freeze-dried and stored in a refrigerator (4°C) for long-term use.

Fabrication of Hydrogels

In a detailed manner, a solution was prepared by dissolving 200 mg of Gelatin methacryloyl (GelMA, GM-60) in 4 mL of PBS containing 0.25 w v^{-1}% LAP. Subsequently, varying amounts of Ag/GO nanoparticles (1 mg mL^{-1}, 2 mg mL^{-1}, and 5 mg mL^{-1}) and GO nanoparticles (3 mg mL^{-1}) were added to the aforementioned solution. The resulting mixture was vigorously stirred for 2 minutes, so that they were fully impregnated, dissolved in a 60–70°C water bath in the dark for 20–30 minutes, oscillated several times during the period, immediately sterilized with 0.22 μm sterile needle filter (to prevent low-temperature gelation), and then crosslinked with UV light for 150 seconds to form. In this study, hydrogels incorporating Ag/GO-GelMA were fabricated and designated as pure GelMA, GG, 1AGG, 2AGG, and 5AGG, respectively. To prevent solidification, all procedures were conducted in the absence of light.

Structural Characterization

The morphology of various samples was examined using a scanning electron microscope (SEM, SU-8010, Hitachi, Japan) and a transmission electron microscope (TEM, JEM-1230, JEOL, Japan). X-ray diffraction (XRD) patterns of graphene oxide (GO) and silver/graphene oxide (Ag/GO) nanoparticles were obtained at an operating voltage of 40 kV and a current of 40 mA, using Cu Kα1 (λ = 0.15418 nm) radiation, in the range of 5° to 80°, utilizing a Bruker AXS D8 Advance diffractometer (Germany). The zeta potentials of the nanoparticles were determined using a ZEN3600 particle size analyzer (Malvern, UK). The UV–vis–NIR absorption spectra were acquired using a Cary5000 spectrophotometer (Agilent, USA). The chemical composition of the samples was analyzed utilizing a Tensor II Fourier transform infrared

(FTIR) spectrometer (Bruker, Germany). Raman spectra were obtained using a Raman spectroscopy instrument (HORIBA Jobin Yvon LabRAM HR). Thermogravimetric analysis (TGA) was conducted employing a thermal gravimetric analyzer (TGA8000, PerkinElmer, USA) with a heating ramp of 10 °C/min from 30 °C to 600 °C under a nitrogen flow. The rheological properties of hydrogels were assessed using a rheometer (DHR-2, TA, USA), and five different rheological tests were conducted: (1) the crosslinking processes of hydrogels were examined by subjecting them to 405 nm UV at a temperature of 25 °C; (2) dynamic strain sweep measurements were conducted to identify the linear viscoelastic regions of the hydrogels; (3) the self-healing behavior of the hydrogels was investigated by determining the storage modulus (G′) and loss modulus (G″) under alternating oscillation strains of 1% and 600%; (4) Dynamic frequency sweep experiments were conducted over a range of 0.1–10 Hz while maintaining a fixed strain of 1% at a temperature of 25 °C; (5) The rheological characteristics of hydrogels at various concentrations were examined through shear rate sweep measurements using an MCR102 instrument (Anton Paar, Austria) with a consistent shear rate of 10 $rads^{-1}$ at a temperature of 25 °C.[34,35,63] The compression strain-stress and elastic modulus were evaluated utilizing a mechanical testing apparatus (Instron 5967, USA) operating at a loading rate of 1 mm min−1 until 60% compression of the hydrogel samples was attained.

Physiochemical Characterization

In order to assess the swelling behavior, the freeze-dried hydrogel specimens were initially weighed and then subjected to incubation in PBS at a temperature of 37 °C until reaching a state of equilibrium. Throughout the swelling process, the hydrogels were periodically extracted at predetermined time intervals, any remaining liquid on the surface of the hydrogels was eliminated using wet filter papers, and the resulting wet weights of the hydrogels (W_w) were measured using an electronic balance (BSA224S-CW, Sartorius, Germany).[21] The swelling ratio was defined as follows:

$$\text{Swelling ratio} = (W_w - W_d)/W_d \tag{4}$$

The mass of the swollen hydrogel specimen is denoted as W_w, while the mass of the initial specimen is represented as W_d.

In order to assess the water retention capacity, freeze-dried hydrogel samples were immersed in PBS until they reached a state of swelling equilibrium (W_0). Following this, the hydrogel specimens at swelling equilibrium were placed in a 37 °C oven, and their masses were measured, with W_w representing the mass of the swollen hydrogel specimen, and Wd representing the mass of the initial specimen. Afterward, the aforementioned swollen equilibrium specimens were relocated to an oven set at a temperature of 37 °C, and their masses (W_t) were measured at various time intervals. The water retention of hydrogels can be computed using the subsequent equation:[21]

$$\text{Water retention}(\%) = \frac{W_t}{W_0} \times 100\% \tag{5}$$

The mass of the hydrogel specimen at a specific time point is denoted as W_t, while W_0 represents the initial mass of the hydrogel.

In Vitro Ag Release

Initially, the 2AGG hydrogel was measured in terms of weight and subsequently submerged in a 40 mL solution of PBS. At predetermined intervals, 4 mL of the PBS solution was extracted and supplemented with an equal volume of fresh PBS buffer. Following this, the Optima 8000 inductively coupled plasma optical emission spectrometry (PerkinElmer, USA) was employed to determine the quantity of silver that had been released. The time points selected for assessing the release of Ag ions were 12, 24, 36, 48, 60, 72, 96, and 120 hours.

The aqueous solution of Ag/GO NPs at a consistent concentration was allowed to stand at room temperature for intervals of 12, 24, 36, 48, 60, 72, 96, and 120 hours, respectively. Subsequently, the supernatant was collected through centrifugation. This procedure was repeated three times to ensure the complete removal of nanoparticles from the supernatant. The mass concentration of the silver element in the supernatant was then measured using the same analytical method to evaluate the efficiency of Ag ions release.

In Vitro Photothermal Performance

The photothermal performance of the prepared samples, namely nanoparticles and hydrogels, was assessed by subjecting them to irradiation from an 808 nm NIR laser. To conduct the evaluation, all samples were placed in 1.5 mL Eppendorf tubes and exposed to the laser at various power settings (0.5, 1.0, and 1.5 W cm^{-2}) for a predetermined duration. The temperatures of the samples were recorded using an E4 FLIR infrared thermometer (USA) during the irradiation process. Additionally, the photothermal stability of the samples was investigated through four cycles of heating and cooling.

In Vitro Antibacterial Evaluation

The in vitro investigation of the antibacterial activity of GelMA-based hydrogels against Staphylococcus aureus (*S. aureus*, ATCC 29213) and Escherichia coli (*E. coli*, ATCC 25922) was conducted using the spread plate method. Hydrogel pieces with a diameter of 8 mm were initially soaked in PBS until absorption equilibrium was reached. Subsequently, they underwent sterilization with a UV lamp for 30 minutes and were then immersed in a bacteria suspension (1 mL, 1.0×10^8 CFU mL^{-1}). Following co-incubation at 37 °C for 4 hours, these samples were subjected to NIR irradiation (808 nm, 0.5 W cm^{-2}) for 3 minutes, with some samples being treated without irradiation. Afterward, a volume of 100 μL of the bacterial solution was extracted from each group and subjected to dilution. Subsequently, 100 μL of the diluted bacterial suspension was evenly distributed onto the newly prepared Luria Bertani broth agar plates. Following overnight incubation, the bacterial colonies on the agar plates were documented and quantified using a J3 colony counter (Tenlin, China). The control group consisted of the bacterial suspension treated with PBS, with or without NIR irradiation. The bacterial survival rates were calculated according to the following equation:[64]

$$Bacterial\ Survival\ rate\ (\%) = \frac{N_t}{N_0} \times 100\% \tag{6}$$

where N_t represents the bacterial number of GelMA, GG, AGG, GG+NIR, and 2AGG+NIR plates, and N_0 represents the bacterial number of PBS plates.

Furthermore, the antibacterial properties of hydrogels were investigated through a bacterial live/dead staining assay. In this assay, the bacteria cells were subjected to various treatments and subsequently co-stained with PI and SYTO9 for a duration of 20 minutes in a light-restricted environment. Following staining, the cells were washed three times with PBS. As per the guidelines provided by the manufacturer, SYTO9 effectively labeled all bacteria, resulting in a green fluorescence, while dead bacteria were stained with PI, exhibiting a red fluorescence. Finally, fluorescence images were captured using confocal laser scanning microscopy (CLSM) with the A1 imaging system manufactured by Nikon in Japan and quantitatively analyzed with Image J. The relative fluorescence ratios were calculated according to the following equation:

$$Relative\ Fluorescence\ Ratio(\%) = \frac{F_1}{F_t} \times 100\% \tag{7}$$

where F_1 represents the red fluorescence (PI) area of PBS, GelMA, GG, 2AGG, and GG+NIR groups, and F_t represents the red fluorescence (PI) area of the 2AGG+NIR group.

All statistical data were analyzed by one-way ANOVA using GraphPad Prism 6.0 statistical software and displayed as bar graphs.

In Vitro Biocompatibility and Cellular Migration Tests

CCK-8 assays were employed to assess the cytotoxicity of the designed hydrogels, namely GelMA, GG, and 2AGG. Prior to conducting the cytotoxicity experiments, the designed hydrogels underwent sterilization using UV light. Subsequently, they were introduced into a DMEM medium containing 10% FBS and 1% P/S for 1, 3, and 5 days to obtain the leaching liquid. Concurrently, HaCAT cells were seeded into a 96-well plate at a density of 1×10^4 cells per well. Following an overnight incubation, the previous cell culture medium was discarded, and the hydrogel extract liquid (100 μL) was added. The HaCAT cells were then cultured for 4 hours. Subsequently, the hydrogel extract liquid was substituted with an equimolar fresh cell culture medium supplemented with 10% CCK-8 for an additional 4 hours of

incubation. Ultimately, the absorbance of the solution at a wavelength of 450 nm was measured using a microplate reader (1530, Thermo Fisher, Finland). The HaCAT cells incubated without hydrogel were utilized as a blank control. Cell viability was determined as follows:

$$\text{Cell viability}(\%) = \frac{A_s}{A_c} \times 100\% \tag{8}$$

where A_s and A_c represent the absorbance values of the hydrogel sample and the control sample at 450 nm, respectively.[65]

Next, the cell viability of the prepared hydrogels (GelMA, GG, and 2AGG) was assessed using a Calcein-AM/PI Cell Viability Kit, following the manufacturer's instructions. HaCAT cells were cultured and seeded as previously described. After treatment with the different groups, the cells in each group were co-stained with Calcein-AM and PI dyes for a duration of 20 minutes. Subsequently, the stained cells were imaged using confocal laser scanning microscopy (CLSM). Following treatment with various groups, the cells in each group were subjected to co-staining with Calcein-AM and PI dyes for a duration of 20 minutes. Subsequently, the stained cells were imaged using confocal laser scanning microscopy (CLSM). The cells that exhibited compromised plasma membranes, indicative of cell death, emitted red fluorescence, while the viable cells that demonstrated esterase activity emitted green fluorescence.

Furthermore, to assess the migratory potential of the hydrogels that were prepared, an in vitro cell scratch assay was conducted. Likewise, the GelMA, GG, and 2AGG hydrogels were subjected to sterilization using UV light and subsequently introduced into a DMEM medium supplemented with 2% FBS for a duration of 3 days to obtain the leaching liquid. Subsequently, HaCAT cells were initially seeded into a 6-well culture plate maintained at a temperature of 37 °C with a CO2 concentration of 5%. The previous cell culture medium in each well was discarded following an overnight incubation period. Subsequently, a 4 mL hydrogel extract liquid was introduced, and a monolayer of cells (with a minimum of 5 parallel lines in each well) was mechanically disrupted using a 200 μL pipet tip. At predetermined time intervals (0, 24, 36, and 48 h), the cells were visually documented using an inverted microscope (IX71, Olympus, Japan).[44]

In Vitro Blood Compatibility

For the analysis of hemolysis, a volume of 1 mL of blood was collected from healthy SD rats using an anticoagulation tube (Konsfi, China). Subsequently, the collected samples were transferred into 2 mL Eppendorf tubes and subjected to centrifugation at 1500 rpm for 15 minutes at a temperature of 4 °C. Following this, the samples were washed three times with 0.9% normal saline solution, and the red blood cells (RBC) were then resuspended in 2 mL of normal saline. Subsequently, 0.8 mL of Triton X-100, PBS, GelMA, GG, and 2AGG were individually added to the prepared RBC suspension. Following a 2-hour incubation period at a temperature of 37 °C, the mixtures underwent centrifugation at a rate of 1500 rpm for a duration of 15 minutes. Subsequently, the supernatant was subjected to spectrophotometric analysis (PE, Enspire, USA) at a wavelength of 540 nm in order to ascertain the concentration of hemoglobin.[60]

In Vivo Photothermal Performance

Male Sprague-Dawley rats were procured from Vital River Laboratory Animal Technology Co., Ltd (Beijing, China). The rats were randomly and equally allocated into six groups, each consisting of three rats: PBS, GelMA, GG, 2AGG, GG + NIR, and 2AGG + NIR. A circular hole measuring 8 mm in diameter was created on the dorsal region of each rat, which was subsequently covered with hydrogels. The wound sites covered with GG and 2AGG hydrogels were subjected to an 808 nm NIR laser irradiation at an intensity of 0.5 W cm^{-2} for a duration of 3 minutes. Thermal images of mouse bodies were captured using a thermal imaging camera.

In Vivo Hemostatic Evaluation

The rats were allocated into five groups (consisting of three rats per group) using random assignment: control, gauze, GelMA, GG, and 2AGG. To initiate the experiment, a surgical scissor was used to remove fifty percent of the length of

the rat tail. Following a 15-second period of bleeding, the wound was promptly covered with the designated samples, and the treated rat was positioned on a pre-weighed dry filter paper. The untreated wound served as the control group.

In Vivo Wound Healing Evaluation

To establish a model of bacteria-infected rat wounds, four circular wounds with a diameter of 8 mm were created on the dorsum of each rat. Following this, 10 μL of *S. aureus* (1.0×10^7 CFU/mL) was immediately applied to the circular wounds and evenly spread across the wound surface. Subsequently, the wounds in each rat were treated with various samples: 200 μL of PBS, GelMA hydrogel, GG hydrogel, 2AGG hydrogel, GG hydrogel + NIR (0.5 W cm^{-2}, 3 min), and 2AGG hydrogel + NIR (0.5 W cm^{-2}, 3 min). A medical tape was used to secure the hydrogels onto the wounds. Photographs of the wounds were acquired using a digital camera at specific time intervals (days 0, 3, 7, and 12). Additionally, to assess the antibacterial efficacy of the treatment, wound secretions were collected on day 3 and cultured on LB agar plates for colony-forming unit (CFU) analysis. On days 7 and 12, the wounds were anesthetized, harvested, fixed in 4% formaldehyde, and subsequently embedded in paraffin. The wound sample sections (5 μm slices) were subjected to staining with Haematoxylin-Eosin (H&E) (Solarbio, G1121, China), Masson staining (Solarbio, G1345, China), Picro Sirius Red, and immunohistochemical (IL-6 and CD31) techniques. The H&E stained sections and Masson staining sections were scanned and analyzed using NIS Viewer image acquisition software, while the immunohistochemical stained sections were scanned and analyzed using Case Viewer image acquisition software.

RNA sequencing, identification of differentially expressed genes, cluster analysis, and functional enrichment analysis

RNA-seq analysis was conducted on rat wound samples obtained from the control and 2AGG+NIR groups at day 12 post-surgery. Each group consisted of a minimum of three samples. TRIzol® Reagent (Invitrogen) was employed to extract total RNA from the tissue samples, following the manufacturer's instructions. DNase I (TAKARA, Japan) was utilized to eliminate genomic DNA. The mRNA expression profiling was performed using the Illumina HiSeqxten/NovaSeq 6000 sequencer. After the final transcriptome was generated, String-Tie and ballgown were used to estimate the expression levels of all transcripts and genes by calculating FPKM [FPKM = total fragments / mapped reads (millions) * exon length(KB)], and the FPKM expression of each sample is $\log_2$ (FPKM+1). Differentially expressed transcripts and genes with a $|\log_2 FC| \geq 1$ and p-value ≤ 0.05, were selected using the DESeq2. Subsequently, a Venn diagram analysis was conducted to compare the differentially expressed genes with the genes identified in the current study on the healing of infectious wounds, utilizing the GeneCards (https://www.genecards.org/) and OMIM-Gene-Map-Retrieval (https://www.omim.org/). Volcano plots were generated using GraphPad Prism 6 to identify genes that exhibited differential expression. The selection of significant differentially expressed genes was based on the Volcano plot analysis. Heatmaps depicting the expression patterns of the selected significant differentially expressed genes were generated using the online bioinformatics tool available at Bioinformatics (http://www.bioinformatics.com.cn/). The construction of the protein-protein interaction (PPI) network for the selected significant differentially expressed genes was accomplished using data from the STRING database and visualized through Cytoscape software version 3.9.1. Furthermore, KEGG pathway enrichment analysis and GO enrichment analysis were conducted using the DAVID Functional Annotation Bioinformatics Microarray Analysis platform (https://david.ncifcrf.gov/).

In Vivo Biosafety Test

Following the completion of in vivo antibacterial and wound healing experiments, blood samples were obtained from rats for subsequent blood biochemistry analysis and blood routine examinations. Concurrently, the major organs (heart, liver, spleen, kidney, and lung) of the rats were extracted and subjected to histological evaluation through staining with hematoxylin and eosin (H&E).

Statistical Analysis

All experiments were repeated a minimum of three times unless otherwise specified. The statistical analysis was carried out utilizing Origin 2021b and GraphPad Prism 6, followed by a Student's test and one-way analysis of variance (ANOVA). A significance level of $*P < 0.05$ was deemed statistically significant, while $**P < 0.01$ and $***P < 0.001$ were considered highly significant.

Conclusion

To summarize, a novel antibacterial platform (Ag/GO-GelMA) was systematically devised and effectively assembled. Initially, Ag/GO nano-PHTAs were synthesized through the growth of Ag nanocrystals on the GO nanoparticles' surface. Subsequently, these nano-PHTAs were uniformly enclosed within a GelMA hydrogel matrix using a straightforward one-pot bending technique. Mechanistically, this study successfully achieved a biologically friendly, simplistic, broad-spectrum, and highly efficient antibacterial platform by exploiting the higher photothermal conversion efficiency of Ag/GO NPs and the inherent bacterial capture/killing ability of the GelMA hydrogel. The antibacterial platform demonstrated remarkable efficacy in killing *E. coli* (99.9%) and *S. aureus* (99.9%) in vitro, as well as superior bactericidal activity in vivo. These findings offer novel insights into the enhancement of the antibacterial performance of GO nano-photothermal agents through material modification and application. In addition, we also demonstrated the effectiveness of the Ag/GO-GelMA hydrogel in uniting NIR from a molecular perspective through transcriptomics. This showed that it can regulate inflammation and promote cell migration, ultimately achieving wound repair and tissue regeneration. In conclusion, our study showed that the Ag/GO-GelMA hydrogel is a very promising and robust antibacterial platform, which provides a simple GO modification strategy capable of extensively improving its PCE and accelerating the healing of infectious wounds, which has made significant progress in the utilization of GO nano-PHTAs.

Data Sharing Statement

The data that support the findings of this work are available from the corresponding author upon reasonable request.

Acknowledgments

Z.S., X.C., and F.M. contributed equally to this work and are co-first authors for this study. This work was financially supported by the Hubei Provincial Central Guidance Local Science and Technology Development Project (2022BGE264), the Health Commission of Hubei Provincial (WJ2023Q017, WJ2023M130), and the Knowledge Innovation Project of Wuhan (2022020801010546, 2023020201020546). All animal experiments conducted in this study were subjected to thorough review and approval by the Institutional Animal Care and Use Committee of Wuhan University (2019-s1211, Wuhan, China). The laboratory animals were handled in accordance with the Guidelines for the Care and Use of Laboratory Animals and the Animal Welfare Act in China.

Author Contributions

Zhiwei Sun: Writing – original draft, Methodology, Data curation, Formal analysis. Xiangru Chen: Writing – original draft, Methodology, Validation, Visualization. Fang Miao: Writing – original draft, Investigation, Software, Resources. Na Meng: Methodology, Software. Keqiang Hu: Conceptualization, Investigation. Shaotang Xiong: Validation, Conceptualization. Ximing Peng: Visualization, Investigation. Liya Ma: Software, Resources. Chuchao Zhou: Writing – review & editing, Supervision, Project ministration, Methodology. Yanqing Yang: Writing – review & editing, Supervision, Funding acquisition, Project ministration, Resources. All authors contributed to data analysis, drafting or revising the article, have agreed on the journal to which the article will be submitted, gave final approval of the version to be published, and agree to be accountable for all aspects of the work.

Disclosure

The authors declare that there is no conflict of interest regarding the publication of this paper.

References

1. Liang Y, Zhao X, Hu T. et al. Adhesive Hemostatic Conducting Injectable Composite Hydrogels with Sustained Drug Release and Photothermal Antibacterial Activity to Promote Full-Thickness Skin Regeneration During Wound Healing. *Small*. 2019;15(12):e1900046. doi:10.1002/smll.201900046
2. El-Aassar MR, Ibrahim OM, Fouda MMG, El-Beheri NG, Agwa MM. Wound healing of nanofiber comprising polygalacturonic/hyaluronic acid embedded silver nanoparticles: in-vitro and in-vivo studies. *Carbohydr Polym*. 2020;238:116175. doi:10.1016/j.carbpol.2020.116175
3. Zhang Y, Li D, Tan J, et al. Near-infrared regulated nanozymatic/photothermal/photodynamic triple-therapy for combating multidrug-resistant bacterial infections via oxygen-vacancy molybdenum trioxide nanodots. *Small*. 2021;17(1):2005739. doi:10.1002/smll.202005739
4. Shafiq M, Yuan Z, Rafique M, et al. Combined effect of SDF-1 peptide and angiogenic cues in co-axial PLGA/gelatin fibers for cutaneous wound healing in diabetic rats. *Colloid Surf B*. 2023;223:113140. doi:10.1016/j.colsurfb.2023.113140
5. Yuan Z, Zhang L, Jiang S, et al. Anti-inflammatory, antibacterial, and antioxidative bioactive glass-based nanofibrous dressing enables scarless wound healing. *Smart Mater Med*. 2023;4:407–426. doi:10.1016/j.smaim.2023.01.001
6. Dong R, Guo B. Smart wound dressings for wound healing. *Nano Today*. 2021;41:101290. doi:10.1016/j.nantod.2021.101290
7. Zheng Q, Liu X, Zheng Y, et al. The recent progress on metal-organic frameworks for phototherapy. *Chem Soc Rev*. 2021;50(8):5086–5125. doi:10.1039/d1cs00056j
8. Lee HP, Gaharwar AK. "Light-responsive inorganic biomaterials for biomedical applications". *Adv Sci*. 2020;7(17). doi:10.1002/advs.202000863
9. Huo J, Jia Q, Huang H, et al. Emerging photothermal-derived multimodal synergistic therapy in combating bacterial infections. *Chem Soc Rev*. 2021;5(15):8762–8789. doi:10.1039/d1cs00074h
10. Jung HS, Verwilst P, Sharma A, et al. Organic molecule-based photothermal agents: an expanding photothermal therapy universe. *Chem Soc Rev*. 2018;47(7):2280–2297. doi:10.1039/c7cs00522a
11. Zhang Y, Liu Y, Guo Z. Chitosan-based bifunctional composite aerogel combining absorption and phototherapy for bacteria elimination. *Carbohydr Polym*. 2020;247:116739. doi:10.1016/j.carbpol.2020.116739
12. Li M, Liang Y, Guo B, Guo B, Guo B. Injectable stretchable self-healing dual dynamic network hydrogel as adhesive anti-oxidant wound dressing for photothermal clearance of bacteria and promoting wound healing of MRSA infected motion wounds. *Chem Eng J*. 2022;427:132039. doi:10.1016/j.cej.2021.132039
13. Petrofsky JS, Lawson D, Berk L, Suh H. Enhanced healing of diabetic foot ulcers using local heat and electrical stimulation for 30 min three times per week. *J Diabetes*. 2010;2(1):41–46. doi:10.1111/j.1753-0407.2009.00058.x
14. Xi Y, Ge J, Wang M, et al. Bioactive anti-inflammatory, antibacterial, antioxidative silicon-based nanofibrous dressing enables cutaneous tumor photothermo-chemo therapy and infection-induced wound healing. *ACS Nano*. 2020;14(3):2904–2916. doi:10.1021/acsnano.9b07173
15. Tan S, Wu X, Xing Y, Lilak S, Wu M, Zhao JX. Enhanced synergetic antibacterial activity by a reduce graphene oxide/Ag nanocomposite through the photothermal effect. *Colloid Surf B*. 2020;185:110616. doi:10.1016/j.colsurfb.2019.110616
16. Wang X, Tian H, Mohammad MA, et al. A spectrally tunable all-graphene-based flexible field-effect light-emitting device. *Nat Commun*. 2015;6(1):7767. doi:10.1038/ncomms8767
17. Chen J, Liu Y, Cheng G, et al. Tailored hydrogel delivering niobium carbide boosts ros-scavenging and antimicrobial activities for diabetic wound healing. *Small*. 2022;18(27):e2201300. doi:10.1002/smll.202201300
18. Yan S, Xu S, Wang Y, et al. A hydrogel dressing comprised of silk fibroin, Ag nanoparticles, and reduced graphene oxide for nir photothermal-enhanced antibacterial efficiency and skin regeneration. *Adv Healthc Mater*. 2024:e2400884. doi:10.1002/adhm.202400884.
19. Li X, Liu L, Li S, et al. Biodegradable π-conjugated oligomer nanoparticles with high photothermal conversion efficiency for cancer theranostics. *ACS Nano*. 2019;13(11):12901–12911. doi:10.1021/acsnano.9b05383
20. Zou Y, Chen X, Yang P, et al. Regulating the absorption spectrum of polydopamine. *Sci Adv*. 2020;6(36). doi:10.1126/sciadv.abb4696
21. Qi X, Huang Y, You S, et al. Engineering robust ag-decorated polydopamine nano-photothermal platforms to combat bacterial infection and prompt wound healing. *Adv Sci*. 2022;9(11):e2106015. doi:10.1002/advs.202106015
22. Cheng D, Bai X, Pan J. In situ hydrothermal growth of cu nps on knitted fabrics through polydopamine templates for heating and sensing. *Chem Eng J*. 2020;382:123036. doi:10.1016/j.cej.2019.123036
23. Shen Y, Zhu C, Chen B. Immobilizing 1-3 nm ag nanoparticles in reduced graphene oxide aerogel as a high-effective catalyst for reduction of nitroaromatic compounds. *Environ Pollut*. 2020;256:113405. doi:10.1016/j.envpol.2019.113405
24. Zeng Q, Qian Y, Huang Y, Ding F, Qi X, Shen J. Polydopamine nanoparticle-dotted food gum hydrogel with excellent antibacterial activity and rapid shape adaptability for accelerated bacteria-infected wound healing. *Bioact Mater*. 2021;6(9):2647–2657. doi:10.1016/j.bioactmat.2021.01.035
25. Jia Z, Lv X, Hou Y, et al. Mussel-inspired nanozyme catalyzed conductive and self-setting hydrogel for adhesive and antibacterial bioelectronics. *Bioact Mater*. 2021;6(9):2676–2687. doi:10.1016/j.bioactmat.2021.01.033
26. Fu Y, Liu L, Zhang L, Wang W. Highly conductive one-dimensional nanofibers: silvered electrospun silica nanofibers via poly(dopamine) functionalization. *ACS Appl Mater Interfaces*. 2014;6(7):5105–5112. doi:10.1021/am5002663
27. Herzog A, Bergmann A, Jeon HS, et al. Operando investigation of ag-decorated Cu_2O nanocube catalysts with enhanced co2 electro reduction toward liquid products. *Angew Chem Int Ed*. 2021;60(13):7426–7435. doi:10.1002/anie.202017070
28. Stone MO, Naik RR, Stringer SJ, Agarwal G, Jones SE. Biomimetic synthesis and patterning of silver nanoparticles. *Nat Mater*. 2002;1(3):169–172. doi:10.1038/nmat758
29. Shin M, Song KH, Burrell JC, Cullen DK, Burdick JA. Injectable and conductive granular hydrogels for 3d printing and electroactive tissue support. *Adv Sci*. 2019;6(20). doi:10.1002/advs.201901229
30. Zhou J, Jiang Y, Hou S, et al. Compact plasmonic blackbody for cancer theranosis in the near-infrared ii window. *Acs Nano*. 2018;12(3):2643–2651. doi:10.1021/acsnano.7b08725
31. Qi X, Pan W, Tong X, et al. E-polylysine-stabilized agarose/polydopamine hydrogel dressings with robust photothermal property for wound healing. *Carbohydr Polym*. 2021;264:118046. doi:10.1016/j.carbpol.2021.118046
32. Nazir F, Ashraf I, Iqbal M, Ahmad T, Anjum S. 6-deoxy-aminocellulose derivatives embedded soft gelatin methacryloyl (gelma) hydrogels for improved wound healing applications: in vitro and in vivo studies. *Int J Biol Macromol*. 2021;185:419–433. doi:10.1016/j.ijbiomac.2021.06.112

33. Rani J, Oh S, Jang J. Raman spectra of luminescent graphene oxide (GO)-phosphor hybrid nanoscrolls. *Materials*. 2015;8(12):8460–8466. doi:10.3390/ma8125470
34. Roth GA, Gale EC, Alcántara-Hernández M, et al. Injectable hydrogels for sustained codelivery of subunit vaccines enhance humoral immunity. *ACS Central Sci*. 2020;6(10):1800–1812. doi:10.1021/acscentsci.0c00732
35. Lai TC, Yu J, Tsai WB. Gelatin methacrylate/carboxybetaine methacrylate hydrogels with tunable crosslinking for controlled drug release. *J Mater Chem B*. 2016;4(13):2304–2313. doi:10.1039/c5tb02518d
36. Li Y, Xu T, Tu Z, et al. Bioactive antibacterial silica-based nanocomposites hydrogel scaffolds with high angiogenesis for promoting diabetic wound healing and skin repair. *Theranostics*. 2020;10(11):4929–4943. doi:10.7150/thno.41839
37. Rastin H, Ormsby RT, Atkins GJ, Losic D. 3d bioprinting of methylcellulose/gelatin-methacryloyl (mc/gelma) bioink with high shape integrity. *ACS Appl Bio Mater*. 2020;3(3):1815–1826. doi:10.1021/acsabm.0c00169
38. Kim H, Chung K, Lee S, Kim DH, Lee H. Near-infrared light-responsive nanomaterials for cancer theranostics. *Wiley Interdiscip Rev Nanomed Nanobiotechnol*. 2016;8(1):23–45. doi:10.1002/wnan.1347
39. Log T. Modeling skin injury from hot spills on clothing. *Int J Environ Res Public Health*. 2017;14(11):1374. doi:10.3390/ijerph14111374
40. Ran L, Lu B, Qiu H, et al. Erythrocyte membrane-camouflaged nanoworms with on-demand antibiotic release for eradicating biofilms using near-infrared irradiation. *Bioact Mater*. 2021;6(9):2956–2968. doi:10.1016/j.bioactmat.2021.01.032
41. Manivannan K, Cheng C, Anbazhagan R, Tsai H, Chen J. Fabrication of silver seeds and nanoparticle on core-shell Ag@SiO2 nanohybrids for combined photothermal therapy and bioimaging. *J Colloid Interface Sci*. 2019;537:604–614. doi:10.1016/j.jcis.2018.11.051
42. Del Castillo-Santaella T, Ortega-Oller I, Padial-Molina M, et al. Formulation, colloidal characterization, and in vitro biological effect of BMP-2 loaded PLGA nanoparticles for bone regeneration. *Pharmaceutics*. 2019;11(8):388. doi:10.3390/pharmaceutics11080388
43. Kurian AG, Singh RK, Patel KD, Lee J, Kim H. Multifunctional gelma platforms with nanomaterials for advanced tissue therapeutics. *Bioact Mater*. 2022;8:267–295. doi:10.1016/j.bioactmat.2021.06.027
44. Cao C, Yang N, Zhao Y, et al. Biodegradable hydrogel with thermo-response and hemostatic effect for photothermal enhanced anti-infective therapy. *Nano Today*. 2021;39:101165. doi:10.1016/j.nantod.2021.101165
45. Wu S, Zhao X, Cui Z, et al. Cytotoxicity of graphene oxide and graphene oxide loaded with doxorubicin on human multiple myeloma cells. *Int J Nanomed*. 2014;9(Issue 1):1413–1421. doi:10.2147/IJN.S57946
46. Liang Y, Li M, Yang Y, Qiao L, Xu H, Guo B. Ph/glucose dual responsive metformin release hydrogel dressings with adhesion and self-healing via dual-dynamic bonding for athletic diabetic foot wound healing. *ACS Nano*. 2022;16(2):3194–3207. doi:10.1021/acsnano.1c11040
47. Yuan Q, Huang J, Xian C, Wu J. Amino acid- and growth factor-based multifunctional nanocapsules for the modulation of the local microenvironment in tissue engineering. *ACS Appl Mater Interfaces*. 2021;13(2):2165–2178. doi:10.1021/acsami.0c15133
48. Zhang S, Hou J, Yuan Q, et al. Arginine derivatives assist dopamine-hyaluronic acid hybrid hydrogels to have enhanced antioxidant activity for wound healing. *Chem Eng J*. 2020;392:123775. doi:10.1016/j.cej.2019.123775
49. Prados ME, Garcia-Martin A, Unciti-Broceta JD, et al. Betulinic acid hydroxamate prevents colonic inflammation and fibrosis in murine models of inflammatory bowel disease. *Acta Pharmacol Sin*. 2021;42(7):1124–1138. doi:10.1038/s41401-020-0497-0
50. Franz S, Ertel A, Engel KM, Simon JC, Saalbach A. Overexpression of S100A9 in obesity impairs macrophage differentiation via TLR4-NFKB-signaling worsening inflammation and wound healing. *Theranostics*. 2022;12(4):1659–1682. doi:10.7150/thno.67174
51. Baldassarro VA, Lorenzini L, Giuliani A, et al. Molecular mechanisms of skin wound healing in non-diabetic and diabetic mice in excision and pressure experimental wounds. *Cell Tissue Res*. 2022;388(3):595–613. doi:10.1007/s00441-022-03624-x
52. Wang W, Yan X, Lin Y, Ge H, Tan Q. Wnt7a promotes wound healing by regulation of angiogenesis and inflammation: issues on diabetes and obesity. *J Dermatol Sci*. 2018;91(2):124–133. doi:10.1016/j.jdermsci.2018.02.007
53. Gaffen SL, Jain R, Garg AV, Cua DJ. IL-23-IL-17 immune axis: discovery, mechanistic understanding, and clinical testing. *Nat Rev Immunol*. 2014;14(9):585–600. doi:10.1038/nri3707
54. Li X, Bechara R, Zhao J, Mcgeachy MJ, Gaffen SL. Interleukin 17 receptor-based signaling and implications for disease. *Nat Immunol*. 2019;20(12):1594–1602. doi:10.1038/s41590-019-0514-y
55. Zegeye MM, Lindkvist M, Fälker K, et al. Activation of the JAK/STAT3 and PI3K/AKT pathways are crucial for IL-6 trans-signaling-mediated pro-inflammatory response in human vascular endothelial cells. *Cell Commun Signal*. 2018;16(1):55. doi:10.1186/s12964-018-0268-4
56. Bao S, Yu D, Tang Z, et al. Conformationally regulated "nanozyme-like" cerium oxide with multiple free radical scavenging activities for osteoimmunology modulation and vascularized osseointegration. *Bioact Mater*. 2024;34:64–79. doi:10.1016/j.bioactmat.2023.12.006
57. Feng Y, Xiao K, Chen J, et al. Immune-microenvironment modulatory polyurethane-hyaluronic acid hybrid hydrogel scaffolds for diabetic wound treatment. *Carbohydr Polym*. 2023;320:121238. doi:10.1016/j.carbpol.2023.121238
58. Zhao Y, Tian C, Liu Y, et al. All-in-one bioactive properties of photothermal nanofibers for accelerating diabetic wound healing. *Biomaterials*. 2023;295:122029. doi:10.1016/j.biomaterials.2023.122029
59. Gao Y, Li Z, Huang J, Zhao M, Wu J. In situ formation of injectable hydrogels for chronic wound healing. *J Mater Chem B*. 2020;8(38):8768–8780. doi:10.1039/d0tb01074j
60. Hu S, Yang Z, Zhai Q, et al. An all-in-one "4A hydrogel": through first-aid hemostatic, antibacterial, antioxidant, and angiogenic to promoting infected wound healing. *Small*. 2023;19(27):e2207437. doi:10.1002/smll.202207437
61. Zhou C, Luo C, Liu S, et al. Pearl-inspired graphene oxide-collagen microgel with multi-layer mineralization through microarray chips for bone defect repair. *Mater Today Bio*. 2022;15:100307. doi:10.1016/j.mtbio.2022.100307
62. Peng X, Liu X, Yang Y, et al. Graphene oxide functionalized gelatin methacryloyl microgel for enhanced biomimetic mineralization and in situ bone repair. *Int J Nanomed*. 2023;18:6725–6741. doi:10.2147/IJN.S433624
63. He J, Sun Y, Gao Q, et al. Gelatin methacryloyl hydrogel, from standardization, performance, to biomedical application. *Adv Healthc Mater*. 2023;12(23):e2300395. doi:10.1002/adhm.202300395
64. Liu L, Lai Y, Cao J, Peng Y, Tian T, Fu W. Exploring the antibacterial and biosensing applications of peroxidase-mimetic ni(0.1)cu(0.9)s nanoflower. *Biosensors*. 2022;12(10):874. doi:10.3390/bios12100874
65. Bortot M, Laughter R, Stein M, Rocker A, Patel V, Park D. Quaternized q-peipaam-based antimicrobial reverse thermal gel: a potential for surgical incision drapes. *ACS Appl Mater Interfaces*. 2018;10(21):17662–17671. doi:10.1021/acsami.8b04020